Special relativity effects on chaos and periodic orbits - a semianalytic approach

Jun-Yin Huang,[1] Hong-Ya Xu,[2,*] Liang Huang,[2,†] and Ying-Cheng Lai[1,3,‡]

[1]*School of Electrical, Computer and Energy Engineering, Arizona State University, Tempe, Arizona 85287, USA*

[2]*Lanzhou Center for Theoretical Physics, Key Laboratory of Theoretical Physics of Gansu Province, Key Laboratory for Quantum Theory and Applications of MOE, and School of Physical Science and Technology, Lanzhou University, Lanzhou, Gansu 730000, China*

[3]*Department of Physics, Arizona State University, Tempe, Arizona 85287, USA*

(Received 28 August 2024; accepted 11 February 2025; published 5 March 2025)

In the study of nonlinear dynamics and chaos, analytically solvable physical models are rare. We investigate the classical motion of a trapped relativistic particle, subject to an electric and a magnetic field. When the directions of the electric and magnetic fields coincide, the dynamics are integrable. As the magnetic field rotates away from the direction of the electric field, a transition to chaos occurs. Based on the approach in a previous work in the nonrelativistic regime [Narimanov *et al.*, Phys. Rev. B **57**, 9807 (1998)], we introduce a particular Lorentz transformation to extend the framework to the relativistic regime, which enables us to derive the Poincaré map and obtain semianalytic formulas for periodic orbits of low periods. The transformation also makes it possible to assess, semianalytically, the role of the degree of the relativistic motion of the particle in its dynamics, revealing that the special relativity effects can enhance chaos. As numerical simulations have played a dominant role in investigating nonlinear physical systems exhibiting chaos and in many cases are the only feasible tool to probe into the system dynamics, our semianalytic approach is unique and leads to additional insights into the interplay between special relativity and chaos.

DOI: 10.1103/PhysRevResearch.7.013241

I. INTRODUCTION

The quest for an analytic understanding of chaos in nonlinear physical systems through exactly solvable models has fascinated physicists for decades, as such an understanding could give the most definitive and satisfactory evidence for various chaos properties of the system under investigation. However, this is challenging as analytically solvable models of nonlinear physical systems are extremely rare even in the nonrelativistic regime. Examples of such models in dissipative dynamical systems include one-dimensional maps [1], the two-dimensional baker's map [2], a system of driven diode resonator [3] comprised of an oscillator, resistor, inductor, and diode in series, which can be reduced exactly to a one-dimensional, noninvertible map. More recently, a statistically solvable quantum model describing memory loss across the integrability–chaos transition under a perturbation obeying no selection rules was articulated [4]. Another class of solvable models of chaos is hybrid systems that typically consist of a linear dynamical system with switchings [5–11]. The solvable models served to provide significant insights into various properties of dissipative chaotic systems. To our knowledge, so far there has been no exactly solvable model for chaos in continuous-time, Hamiltonian systems in the nonrelativistic regime, let alone physical systems in which the special relativity effects cannot be neglected. The purpose of this paper is to present a solvable model of relativistic particle motion in an electric and a magnetic field. A particular phenomenon that we aim to understand semianalytically is the enhanced likelihood of chaos by the special relativity effects.

The effects of relativistic mechanics on classical chaos has been a subject of study in physics [12–25] due to the relevance of this problem to fields such as high-energy and accelerator physics. In an early work [12], it was shown that even a weak relativistic mass effect can lead to enhanced nonlinear effects in systems with a free-electron cyclotron resonance. In a study of the relativistic dynamics of time-driven oscillators [16], it was found that relativistic effects can induce resonances that were absent in the corresponding nonrelativistic system. As resonance overlap can lead to chaos [26], where the emergence of new resonances implies a higher probability of observing chaos in the system. Indeed, subsequently, chaos in special relativistic dynamics was uncovered [18]. In a study of the phase-space structure of the relativistic Sitnikov problem in the first post-Newtonian approximation [21], it was found that transient chaos [27] can emerge. The three-body self-gravitating system was also studied [19,20], revealing the occurrence of chaos. In a relatively recent study of the relativistic anisotropic, two-dimensional harmonic oscillator [23], numerical evidence was presented to support the striking conclusion that *chaos must appear in most integrable classical systems once relativistic corrections are introduced to the dynamics*. Chaos due to the relativistic effect was also found in the motion of high-energy electrons [24]. Quite recently, the Hamilton equations of motion in the limit of weak external

*Contact author: xuhongya@lzu.edu.cn
†Contact author: huangl@lzu.edu.cn
‡Contact author: ying-cheng.lai@asu.edu

field were studied, revealing stronger conditions for integrability when special relativity effects are taken into account [25]. The general consensus from these existing studies is that the special relativity effects tend to increase the likelihood for chaos to arise. To our knowledge, the evidence supporting this proposition has been numerical, with limited or little analytic insights especially in the regime of chaos.

The system of our study is the relativistic motion of a charged particle trapped in a potential, subject to an electric and a magnetic field [28]. The directions of the electric and magnetic fields can be different, and the angle between them is a bifurcation parameter, where zero angle leads to integrable dynamics. As the angle increases from zero, a transition to chaos can occur. While the subject of our study is classical dynamics, it is worth noting that the quantum dynamics of this system were previously studied both theoretically and experimentally [28–41], and a semiclassical theory was developed to understand the experimentally observed spectra [28,30]. The classical dynamics including chaos and periodic orbits of this system were also studied [28,29,40]. All these previous studies concerning this model are for nonrelativistic cases. The key to our success of obtaining a solvable model for this system is a type of Lorentz transform that we articulated, which allows us to derive the Poincaré map and obtain analytic formulas for periodic orbits of low periods. The transform also enables the effects of special relativity on the dynamics to be elucidated, providing semianalytic evidence that relativity enhances chaos.

In Sec. II, we present a physical model of relativistic particle motion in a double potential-well system, subject to an electric and a magnetic field. Two types of motions are introduced: those involving collisions with a single barrier or both barriers [28]. In Sec. III, empowered by a Lorentz boost transform to simplify the particle motion in the electromagnetic fields, we analytically derive the Poincaré maps for both single-barrier and double-barrier dynamics. In particular, the Lorentz transform makes the magnetic field parallel to the electric field so that the periodic orbits can be exactly calculated and their physical origin can be understood. In Sec. IV, we analyze the limit to integrable dynamics. In Sec. V, we carry out a detailed analytic study of periodic orbits of period-1 from single-barrier dynamics in terms of their physical origin, characteristics, stability, bifurcations, and the relativity effects. A brief discussion is presented in Sec. VI.

Additional supporting materials are presented in Appendices. In particular, Appendices A and B give the monodromy matrix for period-1 orbits from single-barrier dynamics and the matrix for period-n orbits from double-barrier dynamics, respectively. Calculation and analysis of period-2 orbits for single-barrier dynamics are presented in Appendix C. A parallel analysis for the periodic orbits from the double-barrier dynamics is detailed in Appendix D.

II. PHYSICAL MODEL: RELATIVISTIC PARTICLE MOTION IN AN ELECTRIC AND A MAGNETIC FIELD

Note that the motion of a relativistic particle in tilted electromagnetic fields is relevant to particle accelerators [42,43], beam transport systems [44], and high-speed particle confinement devices [45]. The field configuration will impact how charged particles are guided, especially when the beam interacts with specific components such as electrodes, plates, or other confinement devices. In addition, the model studied represents the classical correspondence of a quantum well system based on Dirac materials such as HgTe quantum wells [46].

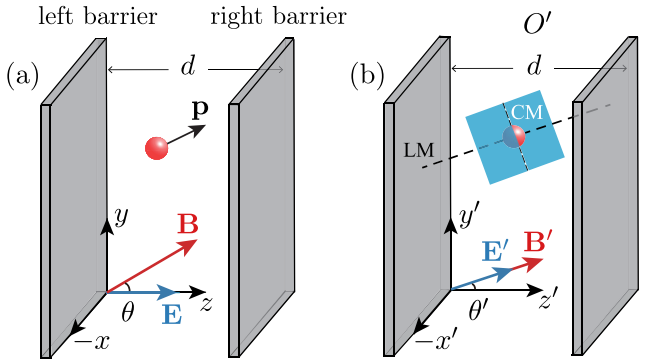

FIG. 1. Schematic illustration of the physical model: a confined relativistic particle subject to an electric and a magnetic field. (a) System setting and coordinates: a relativistic charged particle trapped in a rectangular, double-barrier potential well. The electric field is normal to the potential barriers and the magnetic field is tilted with respect to the electric field with the angle θ. (b) The system in the coordinate frame O' under the Lorentz boost $\Lambda(\widetilde{v})$ along the negative x axis, where $\mathbf{B}'$ is parallel to $\mathbf{E}'$ with the tilted angle θ' to the z' axis. The particle motion in the transformed electromagnetic field can be decomposed into two components: a longitudinal motion and a cyclotron motion, where the former is the relativistic motion under a 1D uniform and static electric field and the latter has the angular frequency $\omega_c'(t') = eB'/m\gamma'(t')$.

A. Relativistic particle equations of motion, Hamiltonian, and Poincaré maps

We consider a charged relativistic particle trapped in a rectangular potential well, as shown in Fig. 1(a), where there is a static electric field and a static magnetic field, and a potential well can be formed involving a single barrier or both barriers. The coordinate conventions are as follows. The potential barrier(s) is (are) located in the (x, y) plane, the electric field $\mathbf{E} = E\hat{\mathbf{z}}$ is in the z direction, and the magnetic field is tilted in the plane (y, z): $\mathbf{B} = B(\sin\theta\hat{\mathbf{y}} + \cos\theta\hat{\mathbf{z}})$. The relativistic equation of motion of the particle in the slanting crossed electromagnetic fields is [47]

$$\mathrm{d}(m\gamma_v\mathbf{v})/\mathrm{d}t = q(\mathbf{v}\times\mathbf{B} + \mathbf{E}), \tag{1}$$

where m is the rest mass, q is the charge, and $\gamma_v = (1 - |\mathbf{v}|^2/c^2)^{-1/2}$. Choosing the mechanical momentum $\mathbf{p} = m\gamma_v\mathbf{v}$ as the dynamical variables, we obtain the following equations of motion for the particle in the free space:

$$\begin{aligned}
\frac{\mathrm{d}p_x}{\mathrm{d}t} &= \frac{qB(p_y\cos\theta - p_z\sin\theta)}{\sqrt{m^2 + p^2/c^2}},\\
\frac{\mathrm{d}p_y}{\mathrm{d}t} &= -\frac{qBp_x\cos\theta}{\sqrt{m^2 + p^2/c^2}},\\
\frac{\mathrm{d}p_z}{\mathrm{d}t} &= \frac{q(Bp_x\sin\theta + E)}{\sqrt{m^2 + p^2/c^2}}.
\end{aligned} \tag{2}$$

Without the potential barriers, these equations are integrable. The dynamical motion of the particle in the potential well thus has two components: a free-space, integrable motion in the electromagnetic fields and elastic collisions with the barriers. The Hamiltonian of the system is

$$H = \sqrt{(\mathbf{P} - q\mathbf{A})^2 c^2 + m^2 c^4} + q\varphi + U(-z) + U(z-d), \tag{3}$$

where $\mathbf{P}$ is the mechanical momentum, the function U is defined as $U(z<0)=0$ and $U(z>0)=\infty$, the vector potential is $\mathbf{A} = (-By\cos\theta + Bz\sin\theta, 0, 0)$, and $\varphi = -Ez$. For electron $q=-e$. For the double barrier well, the left and right barrier walls are located at $z=0$ and $z=d$, respectively, as described by the function U.

Hamiltonian (3) is independent of the coordinate x, so p_x is conserved and the particle dynamics have two degrees of freedom. Using the canonical transformation [28,29]

$$\eta = \frac{y\gamma_0}{c\alpha\omega_0^{-1}} - \frac{P_x}{mc\alpha\cos\theta},\ \zeta = \frac{z\gamma_0}{c\alpha\omega_0^{-1}},$$
$$p_\eta = \frac{P_y}{mc\alpha},\ p_\zeta = \frac{P_z}{mc\alpha}, \tag{4}$$

we arrive at the following dimensionless, effective, two-degrees-of-freedom Hamiltonian:

$$H_{\text{eff}} = \sqrt{1 + \alpha^2\left[p_\eta^2 + p_\zeta^2 + (\eta\cos\theta - \zeta\sin\theta)^2\right]} + \alpha^2\zeta + U(-\zeta) + U\left(\zeta - \frac{d}{c\alpha\omega_0^{-1}}\right) = \gamma_0, \tag{5}$$

with $\omega_0 = eB/m\gamma_0$, incident energy $\epsilon_0 = mc^2\gamma_0$ at $z=0$, $\alpha = E/cB$, and $\gamma_0 = (1 - v_0^2/c^2)^{-1/2}$. To analyze the Hamiltonian dynamics in the canonical coordinates $(\eta, p_\eta; \zeta, p_\zeta)$, we use the Poincaré surface of section method. For $\zeta = 0$ (i.e., $z = 0$), the canonical variable p_ζ can be expressed by η and p_η in terms of the energy conservation of system, and the plane (η, p_η) can be selected as the Poincaré surface of section:

$$v_x = \left.\frac{\partial H}{\partial P_x}\right|_{z=0} = -\frac{c\alpha}{\gamma_0}\cdot\eta,$$
$$v_y = \left.\frac{\partial H}{\partial P_y}\right|_{z=0} = \frac{c\alpha}{\gamma_0}\cdot p_\eta,$$

where the plane (η, p_η) hosting the Poincaré map is equivalent to the plane $(\widetilde{v}_x, \widetilde{v}_y) \equiv (v_x/c, v_y/c)$. Furthermore, the velocity of the particle can be scaled by the modulus of the incident velocity, leading to a scaled Poincaré plane $(\widetilde{v}_x/\widetilde{v}_0, \widetilde{v}_y/\widetilde{v}_0)$.

B. Particle motions involving collisions with a single barrier or double barriers

There are two types of particle motions: one involving collisions with a single barrier and another with both barriers. For convenience, we denote the former as single-barrier dynamics and the latter as double-barrier dynamics. The dimensionless parameter

$$\varrho \equiv m(\gamma_0 - 1)c^2/eEd,$$

defined as the rate of the kinetic energy ϵ_{k0} of the incident particle to the potential difference between the two barriers, provides a criterion to determine if the particle can reach the right barrier. There are two cases. The first is $\varrho \leqslant 1$, where the particle collides only with the left barrier and the dynamics are determined completely by the following three parameters: θ, α, and γ_0, leading to single-barrier dynamics. The second case is $\varrho > 1$, where the particle can collide with both barriers and an additional parameter $d/c\alpha\omega_0^{-1}$ is needed and the dynamics are determined completely by four parameters: θ, α, γ_0, and $d/c\alpha\omega_0^{-1}$, giving rise to double-barrier dynamics. Since

$$d/c\alpha\omega_0^{-1} = (\gamma_0 - 1)/\varrho\alpha^2,$$

ϱ can substitute for the parameter $d/c\alpha\omega_0^{-1}$ as an equivalent parameter for the double-barrier dynamics. For convenience, we call ϱ the swing parameter.

It is worth noting that the swing parameter ϱ degenerates into $\gamma_{\text{NR}} \equiv \epsilon/eEd$ defined for nonrelativistic (NR) motion [28] under the limit $c\to\infty$. Previous works [28–30] also showed that the nonrelativistic dynamics strongly depend on the parameter $\beta_{\text{NR}} \equiv 2v_0B/E$, leading to the parameter $2\widetilde{v}_0/\alpha$ in the relativistic regime. For small $\widetilde{v}_0$, we have $2\widetilde{v}_0/\alpha \approx \beta_{\text{NR}}$, so the weakly relativistic dynamics characterized by $2\widetilde{v}_0/\alpha$ degenerate to the nonrelativistic dynamics as characterized by β_{NR}. Consequently, for fixed $2\widetilde{v}_0/\alpha$, $\widetilde{v}_0$ effectively characterizes the relativity degree of the system.

Consider the single-barrier dynamics as an example. In the nonrelativistic regime, the chaos parameters are θ and $\beta_{\text{NR}} = 2v_0B/E$, where three such parameters arise in the relativistic regime: $\widetilde{v}_0$, θ, and α. To facilitate a comparison between the dynamics in the two regimes, we use the parameters $\widetilde{v}_0$, θ, and $2\widetilde{v}_0/\alpha$ in the relativistic regime, where $2\widetilde{v}_0/\alpha$ replaces the parameter α. As a result, we have $2\widetilde{v}_0/\alpha = \beta_{\text{NR}}$ so that the weakly relativistic dynamics (small $\widetilde{v}_0$) reduce to the nonrelativistic dynamics, making the nonrelativistic dynamics a special case of relativistic dynamics in the limit $\widetilde{v}_0 \to 0$. The relativistic effects thus introduce a new independent "chaos parameter" $\widetilde{v}_0$. The effects of the relativity degree on chaos can be conveniently studied by varying this parameter, while keeping the other parameters (θ and $2\widetilde{v}_0/\alpha$) unchanged. In fact, as shown below (Fig. 3), $\widetilde{v}_0$ is an independent "chaos parameter" that governs the dynamics, greatly facilitating the study of special relativistic effects on chaos. For example, the greater the initial energy of a particle, the larger $\widetilde{v}_0$ becomes and the higher its relativity degree is. The parameter $\widetilde{v}_0$ thus effectively characterizes the relativity degree of the system.

The special relativity factor of the particle at time t depends on the incident energy and $z(t)$:

$$\gamma(t) = \gamma_0 - eEz(t)/mc^2 = \left[\varrho - \frac{z(t)}{d}\right]eEd/mc^2 + 1. \tag{6}$$

To gain insights, we consider two extreme cases: (i) $\varrho \gg 1 > z(t)/d$. and (ii) $\alpha \gg 1$. In the first case, we have $\gamma(t) \approx \gamma_0$ (a constant), giving rise to double-barrier dynamics in the nonrelativistic limit with $m_* = m\gamma_0$. This case was studied previously [28,29]. In the second case, the Poincaré map in

the single-barrier dynamics regime can be written as

$$
\begin{aligned}
(\widetilde{v}_x)_{n+1} &= \left[(\widetilde{v}_x)_n - (\widetilde{v}_y)_n \ln\left(\frac{1+(\widetilde{v}_z)_n}{1-(\widetilde{v}_z)_n}\right)\frac{\cos\theta}{\alpha}\right] f_{\mathrm{SF}},\\
(\widetilde{v}_y)_{n+1} &= \left[(\widetilde{v}_y)_n + (\widetilde{v}_x)_n \ln\left(\frac{1+(\widetilde{v}_z)_n}{1-(\widetilde{v}_z)_n}\right)\frac{\cos\theta}{\alpha}\right] f_{\mathrm{SF}},\\
(\widetilde{v}_z)_{n+1} &= (\widetilde{v}_z)_n,
\end{aligned}
\tag{7}
$$

where n is the discrete time and f_{SF} is the scaling factor. Since $\gamma_{n+1} = \gamma_n$, we have $\widetilde{v}^2_{n+1} = \widetilde{v}^2_n$. Without f_{SF}, Eq. (7) represents the Poincaré map approximate to the first order in $1/\alpha$. After the $(n+1)$th mapping, the change in the velocity squared is

$$
\Delta\widetilde{v}^2 = \left[(\widetilde{v}_x)_n^2 + (\widetilde{v}_y)_n^2\right]\left[\ln\left(\frac{1+(\widetilde{v}_z)_n}{1-(\widetilde{v}_z)_n}\right)\frac{\cos\theta}{\alpha}\right]^2
$$

to the order $(1/\alpha)^2$. This term will accumulate with time n until it can no longer be ignored. This gives the scaling factor f_{SF} as

$$
f_{\mathrm{SF}} = \sqrt{\frac{(\widetilde{v}_x)_n^2 + (\widetilde{v}_y)_n^2}{(\widetilde{v}_x)_{n+1}^2 + (\widetilde{v}_y)_{n+1}^2}}, \tag{8}
$$

so as to ensure $\gamma_{n+1} = \gamma_n$. The distance squared of a point in the Poincaré surface of section from the origin, i.e., $(\widetilde{v}_x^2 + \widetilde{v}_y^2)/\widetilde{v}_0^2$ is given by $1 - \widetilde{v}_z^2/\widetilde{v}_0^2$, so each trajectory must lie on a circle, excluding chaos in this case ($\alpha \gg 1$).

III. LORENTZ BOOST AND POINCARÉ MAP

The analytical solutions for the integrable motion of a relativistic charged particle under uniform electromagnetic fields in the four-dimensional covariant form and three-dimensional notation were obtained previously in Refs. [48–51] and Refs. [52,53], respectively. In the original coordinates O as shown in Fig. 1(a), the solutions are too complicated to be analyzed [48–53]. To make it possible to analyze the particle motion, we apply a Lorentz transformation to obtain the exact form of the Poincaré map, for both single-barrier and double-barrier types of particle motions. The Lorentz boost, denoted as $\Lambda(\widetilde{v})$, describes the change of the space-time coordinates from one inertial frame O to another O' that moves with respect to O along the negative x axis [47], where $\mathbf{B}'$ is parallel to $\mathbf{E}'$ in O', as shown in Fig. 1(b). In particular, for

$$
\widetilde{v}_\pm \equiv v/c = \kappa \pm \sqrt{\kappa^2 - 1}, \tag{9}
$$

the electric and magnetic fields are parallel to each other: $\mathbf{B}'/\!/\mathbf{E}'$, with

$$
\kappa = \frac{\alpha + \alpha^{-1}}{2\sin\theta}. \tag{10}
$$

For $0 \leqslant \theta \leqslant \pi/2$, we have $\kappa \geqslant 1$ so $0 \leqslant \widetilde{v}_- \leqslant 1$ holds, indicating that a Lorentz boost with $\widetilde{v} = \widetilde{v}_-$ can always be found to follow $\mathbf{B}'/\!/\mathbf{E}'$, for arbitrary tilted angle θ in O. In the transformed coordinates, the angle θ' between the vectors $\mathbf{B}'$ (or $\mathbf{E}'$) and the z' axis is given by

$$
\theta' = \arctan\left(\tan\theta - \frac{\alpha\widetilde{v}}{\cos\theta}\right). \tag{11}
$$

We have $-\pi/2 \leqslant \theta' \leqslant \pi/2$, $\theta' < \theta$, $\theta\theta' > 0$, and

$$
B' = \gamma_{\widetilde{v}} B\cos\theta/\cos\theta', \tag{12a}
$$

$$
E' = \gamma_{\widetilde{v}} E(1 - \widetilde{v}\sin\theta/\alpha)/|\cos\theta'|, \tag{12b}
$$

$$
\alpha' = (\alpha - \widetilde{v}\sin\theta)/|\cos\theta|, \tag{12c}
$$

with $\gamma_{\widetilde{v}} = (1-\widetilde{v}^2)^{-1/2}$.

In the new coordinates, the dynamics of the relativistic charged particle are governed by a classic rectangular potential well, subject to the parallel electromagnetic fields with the tilted angle θ' to the barriers in O'. Consider a periodic orbit L of period T_L, starting from the initial position $\mathbf{x}_0$ with the initial scaled velocity $\widetilde{\mathbf{v}}_0$ in O. We have

$$
p^\mu(0) = m\gamma_0 c(1, \widetilde{\mathbf{v}}_0)^t = p^\mu(\tau_1), \tag{13}
$$

$$
x^\mu(\tau_1) = (\mathbf{x}_0, cT_L)^t = x^\mu(0) + (\mathbf{0}, cT_L)^t, \tag{14}
$$

with proper time τ and metric $g_{\mu\nu} = \mathrm{diag}(1,-1,-1,-1)$. Substituting the relations

$$
p^\mu = (\Lambda^{-1})^\mu_\nu p'^\nu \ \text{and} x^\mu = (\Lambda^{-1})^\mu_\nu x'^\nu
$$

into Eqs. (13) and (14), we obtain

$$
p'^\mu(0) = p'^\mu(\tau_1), \tag{15}
$$

$$
\begin{aligned}
x'^\mu(\tau_1) &= x'^\mu(0) + \Lambda(cT_L, \mathbf{0})^t\\
&= x'^\mu(0) + (cT'_L, \mathbf{0})^t,
\end{aligned}
\tag{16}
$$

with $T'_L = \gamma_{\widetilde{v}} T_L$. Equations (15) and (16) indicate that the orbit L' is also a periodic orbit in O'. This suggests a method to analytically find the periodic orbits in the original coordinate system: finding a periodic orbit in O' first and then use the inverse Lorentz boost $\Lambda^{-1}(\widetilde{v})$.

A. Poincaré map for single-barrier motion

We consider another frame of reference O'', rotated by the angle θ' around the x' axis, such that the z'' axis is parallel to the magnetic field:

$$
\begin{aligned}
x'' &= x',\\
y'' &= y'\cos\theta' - z'\sin\theta',\\
z'' &= y'\sin\theta' + z'\cos\theta'.
\end{aligned}
$$

In this reference frame, the integrable motion under the new electromagnetic fields has the following form:

$$
\begin{aligned}
\widetilde{v}_{x''}(\xi) &= (\widetilde{v}_{x''}\cos\xi - \widetilde{v}_{y''}\sin\xi)\gamma''_0/\gamma''(\xi),\\
\widetilde{v}_{y''}(\xi) &= (\widetilde{v}_{y''}\cos\xi + \widetilde{v}_{x''}\sin\xi)\gamma''_0/\gamma''(\xi),\\
\widetilde{v}_{z''}(\xi) &= [\cosh(\alpha'\xi)\widetilde{v}_{z''} - \sinh(\alpha'\xi)]\gamma''_0/\gamma''(\xi),
\end{aligned}
\tag{17}
$$

where $\widetilde{\mathbf{v}}'' = (\widetilde{v}_{x''}, \widetilde{v}_{y''}, \widetilde{v}_{z''})$ is the initial scaled velocity with $\widetilde{v}_{z''} > 0$, $\xi \equiv e\tau B'/m$ is a dimensionless parameter with proper time τ, and

$$
\gamma''_0/\gamma''(\xi) = [\cosh(\alpha'\xi) - \sinh(\alpha'\xi)\widetilde{v}_{z''}]^{-1}. \tag{18}
$$

The integrable dynamics can be decomposed into a longitudinal motion and a cyclotron motion, where the former is the relativistic motion under a 1D uniform and static electric field along the z'' axis governed by the equation $dp_{z''}/dt' = -eE'$, and the latter has the angular frequency $\omega'_c(t') = eB'/m\gamma'(t')$. Note that the cyclotron motion has no effect on the longitudinal motion but the latter affects the angular frequency

of the former through $z''(t')$ and $\gamma'(t')$ directly, with $z''(t')$ determined by the latter completely.

For single-barrier dynamics, the particle collides only with the left barrier. The condition for a collision is

$$z''(\xi_0) - y''(\xi_0)\tan\theta' = 0, \tag{19}$$

where ξ_0 is the first positive real root of the transcendental equation

$$\begin{aligned}\mathcal{F}(\xi;\widetilde{\mathbf{v}}'') &= \sinh(\alpha'\xi)\widetilde{v}_{z''} - \cosh(\alpha'\xi) + 1 \\ &\quad - \alpha'\tan\theta'[\widetilde{v}_{y''}\sin\xi + (1-\cos\xi)\widetilde{v}_{x''}] \\ &= 0,\end{aligned} \tag{20}$$

and the time is

$$t_0' = [\sinh(\alpha'\xi_0) + \widetilde{v}_{z''} - \widetilde{v}_{z''}\cosh(\alpha'\xi_0)]/\omega_0'\alpha'$$

with $\omega_0' = eB'/m\gamma_0'$. The elastic collision can be described by [29]

$$\widetilde{\mathbf{v}}''(\xi_0^+) = \hat{R}_{x''}(2\theta')\hat{T}_{z''}\widetilde{\mathbf{v}}''(\xi_0^-), \tag{21}$$

where $\hat{R}_{x''}(2\theta')$ represents the rotation with the angle $2\theta'$ about the x'' axis, $\hat{T}_{z''} = \mathrm{diag}(1, 1, -1)$ represents the transformation that inverts the direction of $v_{z''}$, and the superscripts "+" and "–" of ξ_0 mark the infinitesimal moment after and before ξ_0, respectively.

In O'', the Poincaré map $\boldsymbol{\mathcal{V}}''$ is

$$\boldsymbol{\mathcal{V}}''(\widetilde{\mathbf{v}}'';\xi_0) = \hat{R}_{x''}(2\theta')\hat{T}_{z''}\widetilde{\mathbf{v}}''(\xi_0). \tag{22}$$

In O, the two-dimensional Poincaré map is explicitly given by

$$\begin{aligned}\mathcal{V}_x &= \frac{\mathcal{V}_x' - \widetilde{v}}{1 - \mathcal{V}_x'\widetilde{v}}, \\ \mathcal{V}_y &= \frac{\mathcal{V}_y'}{\gamma_{\widetilde{v}}(1 - \mathcal{V}_x'\widetilde{v})},\end{aligned} \tag{23}$$

with

$$\begin{aligned}\mathcal{V}_x' &= \mathcal{V}_x'' = \widetilde{v}_{x''}(\xi_0), \\ \mathcal{V}_y' &= \mathcal{V}_y''\cos\theta' + \mathcal{V}_z''\sin\theta' \\ &= \widetilde{v}_{y''}(\xi_0)\cos\theta' + \widetilde{v}_{z''}(\xi_0)\sin\theta'.\end{aligned} \tag{24}$$

B. Poincaré map for double-barrier motion

For $\varrho > 1$, after a collision at the left barrier, the particle can retain enough energy ($\epsilon_{z''}$) to reach the right barrier, leading to motion that involves both barriers. In the phase space, there exists a critical boundary for double-barrier dynamics that separates initial conditions into the left or the right barrier region. Each time the particle collides with the left barrier, we can determine whether the next collision will be with the left or the right barrier. This separates the Poincaré surface of section into different regions.

For $\theta = 0$, i.e., $\widetilde{v} = 0$, the particle has the scaled velocity $\widetilde{\mathbf{v}}_p$ at the moment after the p-th collision with the left barrier. For $(\widetilde{v}_z)_p > \widetilde{v}_z^\dagger$, the particle undergoing the $(p+1)$th integrable motion will collide with the right barrier first, then the $(p+1)$th collision with the left barrier will take place, as determined by $z(t^\dagger, \widetilde{v}_z^\dagger) = d$ with

$$\widetilde{v}_z^\dagger = \sqrt{1 - (1 - 1/\varrho + 1/\varrho\gamma_0)^2}, \tag{25}$$

and $t^\dagger = \widetilde{v}_z^\dagger/\omega_0\alpha$. The critical boundary in the Poincaré surface of section is a circle given by

$$(\widetilde{v}_x/\widetilde{v}_0)^2 + (\widetilde{v}_y/\widetilde{v}_0)^2 = \frac{(1 - 1/\varrho + 1/\varrho\gamma_0)^2 - \gamma_0^{-2}}{1 - \gamma_0^{-2}}, \tag{26}$$

where the right barrier region is inside this circle.

For $\theta \neq 0$, the distance between the two barriers is $d'(=d)$ in the coordinate system O'', and the following condition:

$$z'' - y''\tan\theta' = d'/\cos\theta'$$

is satisfied at the moment of the collision with the right barrier, i.e.,

$$\begin{aligned}\mathcal{F}(\xi;\widetilde{\mathbf{v}}'') &= \sinh(\alpha'\xi)\widetilde{v}_{z''} - \cosh(\alpha'\xi) + 1 \\ &\quad - \alpha'\tan\theta'[\widetilde{v}_{y''}\sin\xi + (1-\cos\xi)\widetilde{v}_{x''}] \\ &= (1 - 1/\gamma_0')/\varrho'\cos\theta',\end{aligned} \tag{27}$$

with

$$\varrho' \equiv \frac{m(\gamma_0' - 1)c^2}{eE'd'} = \frac{\alpha(\gamma_0' - 1)\cos\theta'}{\alpha'\gamma_{\widetilde{v}}(\gamma_0 - 1)\cos\theta}\cdot\varrho. \tag{28}$$

Denote the scaled velocity at the moment after the pth collision with the left barrier as

$$\widetilde{\mathbf{v}}'' = (\widetilde{v}_{x''}, \widetilde{v}_{y''}, \widetilde{v}_{z''}).$$

The conditions for the particle to reach the right barrier before the next collision with the left battier are: ξ_r exists and $\xi_r < \xi$, where ξ_r and ξ are the first positive real roots of Eqs. (27) and (20), respectively. For $\theta \neq 0$, the critical boundary depends on the parameters γ_0, θ, α, and ϱ, which can be obtained by substituting

$$\begin{aligned}\widetilde{v}_{x''} &= \frac{\widetilde{v}_x + \widetilde{v}}{1 + \widetilde{v}_x\widetilde{v}}, \\ \widetilde{v}_{y''} &= \frac{\widetilde{v}_y\cos\theta' - \widetilde{v}_z\sin\theta'}{\gamma_{\widetilde{v}}(1 + \widetilde{v}_x\widetilde{v})}, \\ \widetilde{v}_{z''} &= \frac{\widetilde{v}_y\sin\theta' + \widetilde{v}_z\cos\theta'}{\gamma_{\widetilde{v}}(1 + \widetilde{v}_x\widetilde{v})},\end{aligned}$$

into Eq. (27) to determine whether the particle with $\widetilde{\mathbf{v}}$ can collide with the right barrier first.

Two examples of the critical boundary are shown in Fig. 2. It can be seen that the value of ϱ affects the size of the right barrier region. In fact, θ affects the position of the critical boundary through θ' directly, where a larger angle θ' corresponds to more deviation of the critical boundary from the origin. Similarly, α affects the position of the critical boundary through θ'. The size of the right barrier region increases with ϱ (major effect) but decreases with $\widetilde{v}_0$, θ, and α (minor effect). As the degree of relativity continues to increase, and the critical boundary tends to reach some certain shape in the weakly relativistic or ultra-relativistic regime, where the size of the right barrier region tends to a certain nonzero value, as shown in Fig. 2(b). In general, the particle trajectory can cross the critical boundary as the parameters change, especially in the case of large chaotic seas where nearly all trajectories are ergodic.

We can now obtain the Poincaré map for double-barrier dynamics. The particle with the scaled velocity $\widetilde{\mathbf{v}}_p''$ leaves the

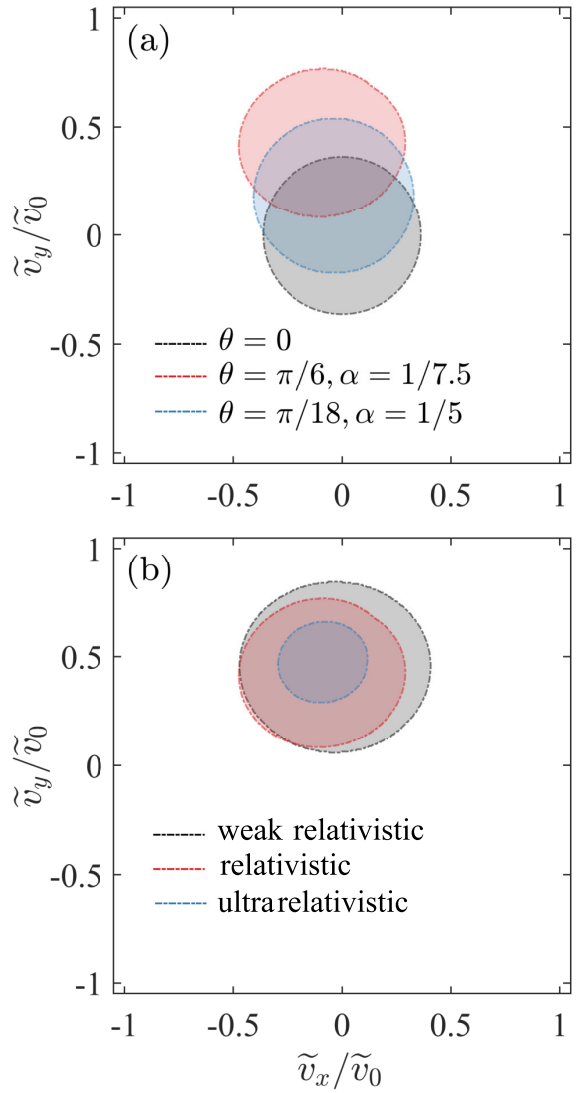

FIG. 2. Two examples of the critical boundaries for particle motion that involves two barriers. In each example, the critical boundaries for three different cases are displayed: weakly relativistic, relativistic, and ultrarelativistic. (a) The parameter values are $\varrho = 1.2$, $\widetilde{v}_0 = 0.8$, $\theta = 0$ (black), $\theta = \pi/6$, $\alpha = 1/7.5$ (red), $\theta = \pi/18$, and $\alpha = 1/5$ (blue). (b) The parameter values are $\varrho = 1.2$, $\theta = \pi/6$, $2\widetilde{v}_0/\alpha = 12$, $\widetilde{v}_0 = 0.0008$ (black), $\widetilde{v}_0 = 0.8$ (red), and $\widetilde{v}_0 = 0.999$ (blue). The right barrier region is colored while the left barrier region is blank.

pth point on the Poincaré surface of section at the moment after the pth collision with the left barrier. If $\widetilde{\mathbf{v}}''_p$ is located in the left barrier region, the $(p+1)$th integrable motion in the space can be described by $\boldsymbol{\mathcal{V}}''$, otherwise the $(p+1)$th integrable motion contains two segments: the first is the particle reaching the right barrier after the pth collision with the left barrier and then experiencing a collision with the right barrier, and the second is the particle's reaching the left barrier after the collision with the right barrier and then experiencing the $(p+1)$th collision with the left barrier.

For the first segment, the integrable motion is governed by the motion parameter ξ_r. Immediately after a collision with the right barrier, the scaled velocity can be written as

$$\widetilde{\mathbf{v}}''_r = \boldsymbol{\mathcal{V}}''(\widetilde{\mathbf{v}}''; \xi_r) = \hat{R}_{x''}(2\theta')\hat{T}_{z''}\widetilde{\mathbf{v}}''(\xi_r^-),$$

where $\widetilde{\mathbf{v}}''(\xi_r^-)$ is the scaled velocity immediately before the collision as given by Eq. (20). Moreover, we have

$$\widetilde{v}^r_{z''} = -\sqrt{1 - \left[\frac{(1-\widetilde{v}^r_{x''}\widetilde{v})\gamma_{\widetilde{v}}\varrho}{\gamma_0(\varrho-1)+1}\right]^2 - \left(\widetilde{v}^r_{x''}\right)^2 - \left(\widetilde{v}^r_{y''}\right)^2}$$

which is obtained by simplifying

$$\gamma_r = [\gamma_0(\varrho-1)+1]/\varrho = \gamma''(\xi_r)\gamma_{\widetilde{v}}(1-\widetilde{v}^r_{x''}\widetilde{v}), \tag{29}$$

where γ_r is the relativity factor when the particle reaches the right barrier.

For the second segment, the relativity factor is no longer γ'_0 but $\gamma'(\xi_r)$, so the motion parameter ξ_l is the first positive real root of

$$\mathcal{F}(\xi; \widetilde{\mathbf{v}}''_r) + (\gamma'_0 - 1)/\gamma'(\xi_r)\varrho' \cos\theta' = 0, \tag{30}$$

where

$$\gamma'_0/\gamma'(\xi_r) = 1/[\cosh(\alpha'\xi_r) - \sinh(\alpha'\xi_r)\widetilde{v}_{z''}].$$

Similar to the first segment, the quantity

$$\widetilde{\mathbf{v}}''_{p+1} = \boldsymbol{\mathcal{V}}''(\widetilde{\mathbf{v}}''_r; \xi_l)$$

represents the scaled velocity at the moment after the $(p+1)$th collision with the left barrier.

C. Special relativity effects enhance Hamiltonian chaos

Figure 3 presents examples of the system dynamics on the Poincaré map defined by the scaled and normalized velocities in the x and y directions, for different relativity degrees: [(a) and (e)] weakly relativistic, [(b) and (f)] relativistic, [(c) and (g)] strongly relativistic, and [(d) and (h)] ultrarelativistic. The phase-space plots of the dynamics associated with single-barrier and double-barrier dynamics are shown in Figs. 3(a)–3(d) and 3(e)–3(h), respectively. In all cases, we observe the typical mixed phase-space structure of Hamiltonian systems: coexistence of Kolmogorov–Arnold–Moser (KAM) tori and chaotic seas. As the degree of special relativity increases, chaotic layers begin to emerge [Figs. 3(b) and 3(f)] and the chaotic sea gradually expands until it fills almost the entire Poincaré surface of section [Figs. 3(d) and 3(h)]. That is, special relativity effects enhance chaos! It is worth emphasizing that chaos originates from the non-head-on elastic collisions with the barriers. In our system, the nonrelativistic dynamics are already chaotic for $\theta \neq 0$ but relativistic effects serve to enhance chaos, as demonstrated in Fig. 3, which is different from some related works [12–18]. We also note the nature of our semianalytic approach: the results in Fig. 3 are obtained numerically directly from the Poincaré maps that are analytically derived, not from numerically solving the Hamilton's equations of motion (i.e., a set of nonlinear differential equations).

For double-barrier dynamics, in the coordinate system O'', the Poincaré map is

$$\boldsymbol{\mathcal{V}}''_{\mathrm{D}} = \boldsymbol{\mathcal{V}}''(\widetilde{\mathbf{v}}''_r; \xi_l). \tag{31}$$

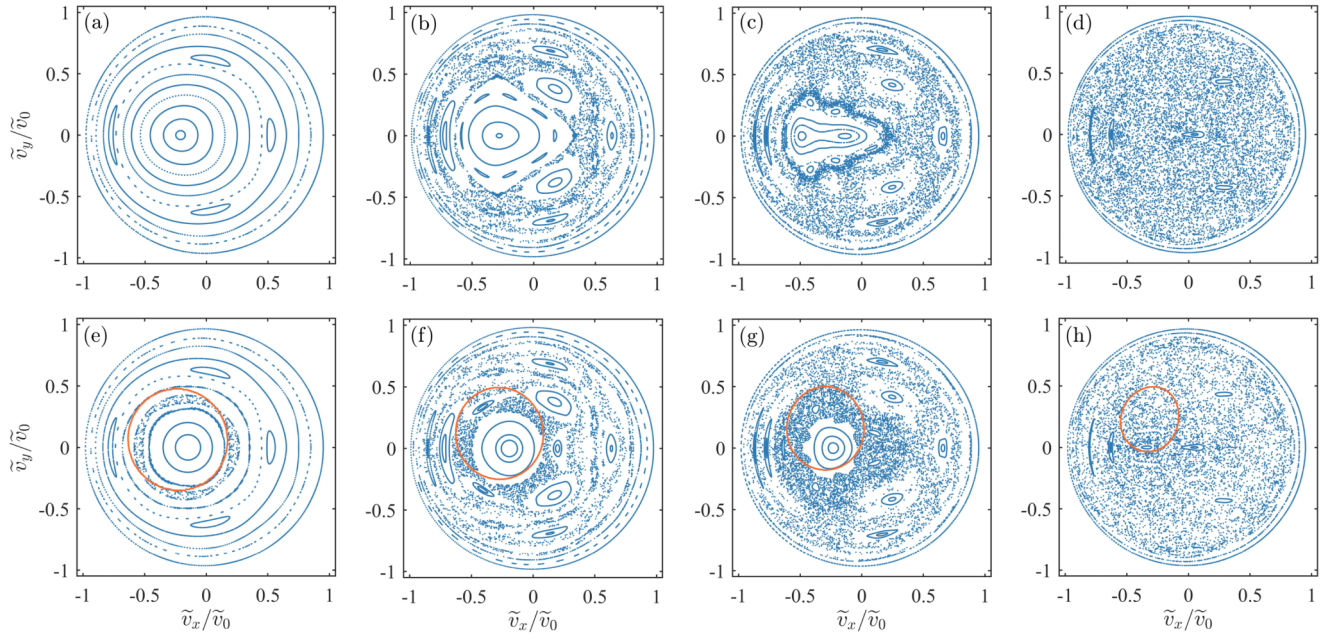

FIG. 3. Chaotic dynamics on the Poincaré surfaces of section for different relativity degrees. [(a)–(d)] Single-barrier and [(e)–(h)] Double-barrier dynamics for $\varrho = 1.2$. Other parameters are $2\widetilde{v}_0/\alpha = 12/5$ and $\theta = \pi/6$. For fixed $2\widetilde{v}_0/\alpha$, the relativity degree can be conveniently represented by the incident velocity $\widetilde{v}$: [(a) and (e)] $\widetilde{v}_0 = 0.08$ (weakly relativistic), [(b) and (f)] $\widetilde{v}_0 = 0.8$ (relativistic), [(c) and (g)] $\widetilde{v}_0 = 0.92$ (strongly relativistic), and [(d) and (h)] $\widetilde{v}_0 = 0.99$ (ultrarelativistic). The orange solid curves in (e)–(h) mark the boundary for double-barrier dynamics. All displayed Poincaré maps exhibit typical features of a Hamiltonian phase space: coexistence of KAM tori/islands and chaotic sea. As the system becomes more relativistic, chaos is enhanced characterized by a continuous increase in the area of the chaotic sea on the Poincaré map.

In the relativistic regime, on the Poincaré surface of section, there are regions of "chaotic halo" for small chaos parameter and small θ, as exemplified in Figs. 3(d)–3(f). The difference between such a chaotic halo and some distorted KAM tori are relatively pronounced in Figs. 3(d) and 3(f). Here, the innermost KAM torus is determined by $\boldsymbol{\mathcal{V}}''_{\mathrm{D}}$ only, i.e., there must be a collision with the right barrier before each collision with the left barrier. The outermost KAM torus is determined by (1) the existence of $\boldsymbol{\mathcal{V}}''$ and (2) the derivative of the Poincaré map with respect to $\widetilde{\mathbf{v}}''$ being discontinuous once the trajectory crosses the critical boundary. Note that chaotic halo regions similar to those in Figs. 3(d)–3(f) also exist in nonrelativistic particle dynamics [28].

Overall, chaos originates from non-head-on elastic collisions with the barriers. While the motion of a charged nonrelativistic particle in electromagnetic fields is integrable, relativistic effects can make the motion more complicated. In our system, after applying an appropriate Lorentz transformation ($O \to O'$), $\mathbf{B}'$ becomes parallel to $\mathbf{E}'$. In this frame, the motion involves acceleration followed by deceleration along the direction of $\mathbf{E}'$, accompanied by cyclotron motion in the plane perpendicular to $\mathbf{E}'$. Due to the relativistic effects, the cyclotron frequency is no longer constant but varies with the particle's position along the $\mathbf{E}'$ direction. More specifically, the effective Hamiltonian

$$H_{\mathrm{eff}} = \sqrt{1+\alpha^2\left[p_\eta^2 + p_\zeta^2 + (\eta\cos\theta - \zeta\sin\theta)^2\right]} + \alpha^2\zeta + U(-\zeta) + U\left(\zeta - \frac{d}{c\alpha\omega_0^{-1}}\right) = \gamma_0,$$

includes a more complex square root structure. For small α, the Hamiltonian can be reduced to the nonrelativistic one by ignoring terms of orders higher than α^2. The relativistic Hamiltonian preserves the higher-order effects, leading to enhancement of chaos.

IV. ANALYTIC SOLUTION OF INTEGRABLE DYNAMICS

As a prelude to analytically calculating periodic orbits to gain insights, we analyze the integrable dynamics that arise when the electric and magnetic fields are in the same direction ($\theta = 0$). In this case, the particle dynamics in between two adjacent collisions can be decomposed into two components: longitudinal motion along the z axis and cyclotron motion in the plane (x, y). All periodic orbits can be divided into two groups: a single traversing orbit bouncing perpendicular to the barrier(s) with $\mathbf{v}_0 = v_z\hat{\mathbf{z}}$ (i.e., a pure longitudinal motion) and infinite families of helical orbits whose radius of the cross section within the (x, y) plane depends on $z(t)$.

We first analyze orbits arising from single-barrier dynamics. The fixed point (0,0) of the Poincaré map represents a traversing orbit with the period

$$T_{\mathrm{TO}} = \frac{2\left(1-\gamma_0^{-2}\right)^{1/2}}{\omega_0\alpha}. \tag{32}$$

A helical orbit can be decomposed into a longitudinal and a cyclotron motion component. For single-barrier dynamics, if the period of a family of helical orbits is

$$T = nT_{\mathrm{CM}} = nT_{\mathrm{TO}}\widetilde{v}_z/\widetilde{v}_0, \tag{33}$$

the corresponding phase change $\Delta\theta_c$ is given by

$$\Delta\theta_c = n\int_0^{T_{\rm CM}} \omega_c(t)dt = \frac{neB}{m}\int_0^{T_{\rm CM}} \frac{dt}{\gamma_0 - eEz(t)/mc^2} = \frac{n}{\alpha}\ln\left(\frac{1+\widetilde{v}_z}{1-\widetilde{v}_z}\right) \tag{34}$$

where $\widetilde{v}_z$ is the component of initial scaled velocity along the z axis. The phase change can be obtained by using

$$z(t) = \frac{m\gamma_0 c^2}{eE}\left[1-\sqrt{1-\widetilde{v}_z^2+(\alpha\omega_0 t-\widetilde{v}_z)^2}\right]. \tag{35}$$

The family of helical orbits determines the resonant torus via the resonance condition $\Delta\theta_c = 2k\pi$ with positive integers n and k. When n and k do not have a common divisor, both the helical-orbit family and the resonant torus can be conveniently denoted as $\{n,k\}$, stipulating that the orbit returns to the initial state through n collisions with the left barrier and k whole cyclotron rotations (corresponding to a periodic orbit of period-n in the Poincaré map). Giving the initial energy $m\gamma_0 c^2$, this family of periodic orbits satisfies the following condition:

$$\widetilde{v}_z = \frac{\exp(2\pi\alpha k/n)-1}{\exp(2\pi\alpha k/n)+1} \tag{36}$$

for single-barrier dynamics located at an invariant torus with $R=\sqrt{\widetilde{v}_0^2-\widetilde{v}_z^2}$ denoted as $\{n,k\}$. For periodic orbits with the initial energy $m\gamma_0 c^2$ to arise, in addition to the requirement $\widetilde{v}_z \leqslant \widetilde{v}_0$, another condition needs to be met:

$$\frac{k}{n} \leqslant \frac{1}{2\pi\alpha}\ln\left(\frac{1+\widetilde{v}_0}{1-\widetilde{v}_0}\right). \tag{37}$$

We next consider orbits from double-barrier dynamics. A traversing orbit with $z(t=T_{\rm TO}/2)=d$ has the period

$$T_{\rm TO} = \frac{2\left(1-\gamma_0^{-2}\right)^{1/2}}{\omega_0\alpha}\left(1-\sqrt{\frac{\varrho-1}{\varrho}\left[1+\frac{1-\gamma_0}{(1+\gamma_0)\varrho}\right]}\right). \tag{38}$$

In the nonrelativistic case, the period becomes

$$\lim_{c\to\infty} T_{\rm TO} = \frac{\beta_{\rm NR}}{\omega_0}\left(1-\sqrt{1-\frac{1}{\gamma_{\rm NR}}}\right). \tag{39}$$

For the family of helical orbits $\{n,k\}$, the phase change is given by

$$\Delta\theta_c = \frac{2n}{\alpha}\ln\left(\frac{1+\widetilde{v}_z}{\gamma_r/\gamma_0+\sqrt{\gamma_r^2/\gamma_0^2+\widetilde{v}_z^2-1}}\right) = 2k\pi \tag{40}$$

for $\gamma_r/\gamma_0 = 1-1/\varrho+1/\varrho\gamma_0$. Giving the initial energy $m\gamma_0 c^2$, we have

$$\widetilde{v}_z = \frac{\exp(2\pi\alpha k/n)+1-2\gamma_r\exp(\pi\alpha k/n)/\gamma_0}{\exp(2\pi\alpha k/n)-1}.$$

We now present examples of the family of periodic orbits denoted as $\{n,k\}$. For single-barrier dynamics, a left barrier orbit is one which can never reach the right barrier, as stipulated by Eq. (36):

$$\alpha_{\rm SBM} = n\ln\left[(1+\widetilde{v}_z)/(1-\widetilde{v}_z)\right]\big/2\pi k.$$

The smaller $1/\alpha$ is, the larger longitudinal scaled velocity $\widetilde{v}_z$, the larger the longitudinal maximum displacement, and the closer the orbit is to the right barrier. When $1/\alpha$ decreases to the critical value $1/\alpha^\dagger$, $\widetilde{v}_z$ will increase to the critical value $\widetilde{v}_z^\dagger$ so the particle can reach the right barrier with

$$\alpha^\dagger = \alpha_{\rm SBM}(\widetilde{v}_z^\dagger) = \frac{n}{\pi k}\ln\left(\frac{1+\sqrt{1-\gamma_r^2/\gamma_0^2}}{\gamma_r/\gamma_0}\right), \tag{41}$$

i.e., the left barrier periodic orbit $\{n,k\}$ exists in the range $1/\alpha \geqslant 1/\alpha^\dagger$, as illustrated in Fig. 4.

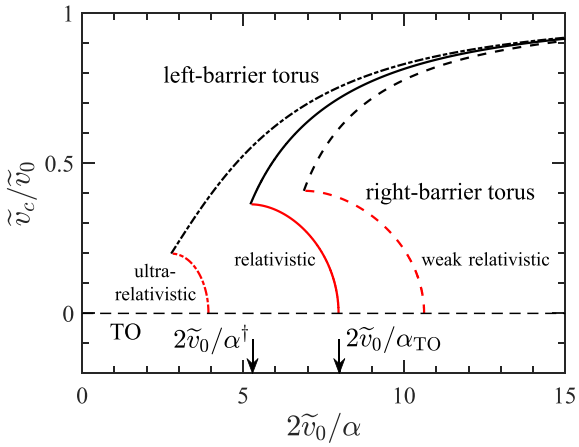

FIG. 4. Scaled cyclotron velocity for the resonant torus $\{1,1\}$ as a function of $2\widetilde{v}_0/\alpha$ for the integrable dynamics with $\theta=0$. The value of the swing parameter is $\varrho=1.2$. Shown are the functions of the scaled cyclotron velocity for three initial-velocity values: $\widetilde{v}_0 = 0.0008$ (weakly relativistic, dashed curves), $\widetilde{v}_0 = 0.8$ (relativistic, solid curves), and $\widetilde{v}_0 = 0.999$ (ultra-relativistic, dash-dotted curves). The left and the right barrier tori are denoted by black and red, respectively. The horizontal dashed line $\widetilde{v}_c = 0$ corresponds to the traversing orbit, and the arrows indicate the upper and lower boundaries of $2\widetilde{v}_0/\alpha$ for the case of relativistic motion.

For double-barrier dynamics, the right barrier orbit can be defined in a similar way. A right barrier torus in the Poincaré map is determined by the corresponding right-barrier periodic orbit $\{n,k\}$ with

$$\alpha_{\rm DBM} = \frac{n}{\pi k}\ln\left(\frac{1+\widetilde{v}_z}{\gamma_r/\gamma_0+\sqrt{\gamma_r^2/\gamma_0^2+\widetilde{v}_z^2-1}}\right). \tag{42}$$

Since $\partial\alpha_{\rm DBM}/\partial\widetilde{v}_z < 0$, the smaller $1/\alpha$ is, the smaller $\widetilde{v}_z$ will be (contrary to the single-barrier dynamics case). The right barrier torus $\{n,k\}$ has its longitudinal scaled velocity limited in the range $\widetilde{v}_z^\dagger < \widetilde{v}_z \leqslant \widetilde{v}_0$, and $1/\alpha$ is restricted to the range of $1/\alpha^\dagger < 1/\alpha \leqslant 1/\alpha_{\rm TO}$, where $\alpha_{\rm TO} = \alpha_{\rm DBM}(\widetilde{v}_0)$ are associated with the traversing orbit, as shown in Fig. 4.

When $1/\alpha$ increases through $1/\alpha^\dagger$, the left and right barrier torus simultaneously appear in the adjacency domain of the critical boundary for double-barrier dynamics with a given

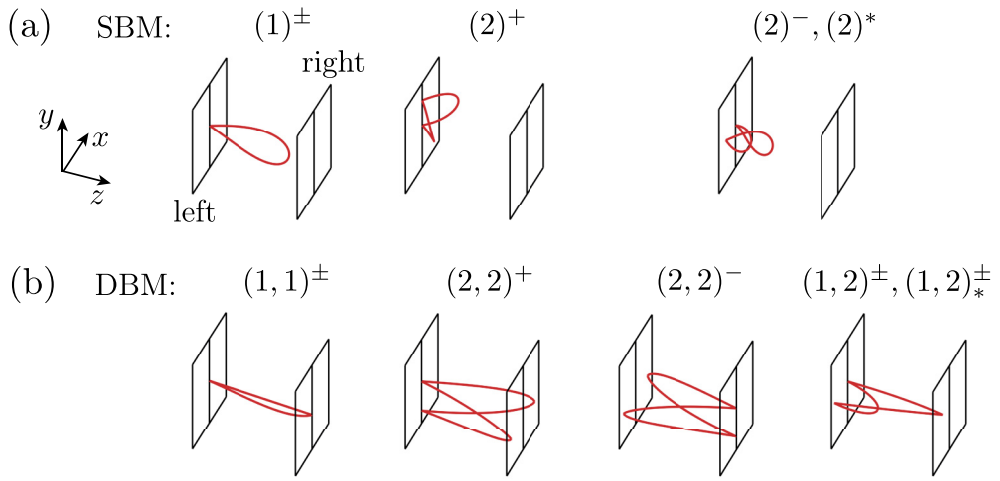

FIG. 5. Representative periodic orbits in the relativistic dynamical system governed by the Hamiltonian (3). (a) Periodic orbits formed by the particle's interacting with a single potential barrier: period-1 orbits $(1)^{\pm}$, type-A period-2 orbits $(2)^{+}$, and type-B period-2 orbits $(2)^{-}$ and $(2)^{*}$. (d) Examples of periodic orbits requiring interaction with both barriers: period-1 orbits $(1, 1)^{\pm}$, period-2 orbits $(2, 2)^{+}$ [deformed from $(2)^{+}$], $(2, 2)^{-}$ and $(1, 2)^{\pm}$ [deformed from $(2)^{-}$], and $(1, 2)^{\pm}_{*}$ [deformed from $(2)^{*}$] in the double-barrier well. The "±" sign indicates initially stable (+) or unstable (–) periodic orbits.

value of the swing parameter ϱ. The left and right barrier tori keep expanding and shrinking, respectively, from the critical boundary until they are close to the unit circle centered at (0,0). By continuity [54], some pairs of periodic orbits survive through the destruction process of the tori when the magnetic field has a infinitesimal tilt, where the formation and evolution of the left barrier periodic orbits are the same as those with single-barrier dynamics. Unique to double-barrier dynamics are thus the right barrier periodic orbits.

The relativistic nature of the motion is controlled by the parameter $\widetilde{v}_0$, so a useful dynamic parameter is $2\widetilde{v}_0/\alpha$. As shown in Fig. 4, as this parameter increases, the parameter region permitting the right barrier torus reduces, and the upper and lower bounds of the left and right barrier tori correspond to a smaller value of $2\widetilde{v}_0/\alpha$. It can then be anticipated that the dynamics in the relativistic and nonrelativistic cases share similar qualitative features. As will be discussed below, this result is also supported by a detailed analysis of the periodic orbits from both single-barrier and double-barrier dynamics in terms of their types and stability.

V. ANALYTIC SOLUTIONS OF PERIODIC ORBITS FROM SINGLE-BARRIER DYNAMICS

Now we turn to analyze the nonintegrable dynamics that arise when the electric and magnetic fields are in different directions ($\theta \neq 0$). In nonlinear dynamical systems, periodic orbits are fundamental to the physically observable phenomena, where the system behaviors are determined by the dynamical invariant sets that can be periodic or chaotic. In dissipative dynamical systems, chaotic attractors are attracting, dynamically invariant sets contain an infinite set of unstable periodic orbits [2], while nonattracting chaotic invariant sets lead to transient chaos [27]. Invariant measures, the fundamental characterization of any chaotic set, are supported by the infinite set of unstable periodic orbits [55–58]. While there were efficient numerical algorithms for calculating the unstable periodic orbits in dissipative chaotic systems [59,60], analytically finding periodic orbits has always been challenging, especially for Hamiltonian systems.

We have succeeded in analytically calculating the periodic orbits of low periods in the relativistic dynamical system governed by the Hamiltonian (3). Some representative periodic orbits are shown in Fig. 5, for both the single-barrier and double-barrier dynamical regimes. While the basic methodology underlying our analysis is the same for finding the periodic orbits in the single-barrier and double-barrier dynamical regimes, the details are different. We detail our calculation and analysis of the period-1 orbits for single-barrier dynamics here, while presenting the results of period-2 orbits in Appendix C. The corresponding results from the double-barrier dynamics are described in Appendix D.

A. Solutions of period-1 orbits

Period-1 orbits are typically helical orbits $\{1, k\}$, as the traversing motion with the initial velocity $\mathbf{v}'_0 = v'_0(1, \sin\theta', \cos\theta')$ has the velocities

$$\mathbf{v}'(T^{-}_{\rm TO}) = -\mathbf{v}'_0,$$
$$\mathbf{v}'(T^{+}_{\rm TO}) = v'_0(1, -\sin\theta', \cos\theta') \neq \mathbf{v}'_0$$

immediately before and after the elastic collision with the left barrier, respectively. For the traversing motion to have a periodic behavior, the condition $\theta' = 0$ (i.e., $\theta = 0, \pm\pi/2$) must be met. In this case, the fixed point of the Poincaré map is $(\widetilde{v}^{*}_{x}, \widetilde{v}^{*}_{y}) = (-\widetilde{v}, 0)$, denoted as $\{1, 0\}$. For an infinitesimally tilted magnetic field ($\theta' \neq 0$), this periodic orbit is destroyed. Our analysis will focus on periodic orbits associated with the helical motion.

We study the family of helical motions in the coordinate system O''. For clarity, we denote the fixed point by "$*$" in all the reference frames. Letting T_* be the period in O'',

we have

$$\begin{aligned} v_{x'}(T_*^-) &= v_{x''}(T_*^-) = v_{x'}^*, \\ v_{y'}(T_*^-) &= v_{y''}(T_*^-)\cos\theta' + v_{z''}(T_*^-)\sin\theta' = v_{y'}^*, \\ v_{z'}(T_*^-) &= -v_{y''}(T_*^-)\sin\theta' + v_{z''}(T_*^-)\cos\theta' = -v_{z'}^*. \end{aligned} \quad (43)$$

Replacing the expression of initial velocity in O' with that in O'': $v_{z''}(T_*^-) = -v_{z''}^*$, we have

$$v_{x''}(T_*^-) = v_{x''}^*,\ v_{y''}(T_*^-) = -v_{y''}^*,\ v_{y'}^* = 0. \quad (44)$$

As a result, the initial velocity $\mathbf{v}_0'' = (v_0'', \phi'', \varphi'')$ with $v_{y''}^* = -v_{z''}^* \tan\theta'$ (due to $v_{y'}^* = 0$) satisfies

$$\sin\varphi'' = -\frac{\tan\theta'}{\sqrt{(v_0''/v_{z''}^*)^2 - 1}}, \quad (45)$$

with the phase change

$$\Delta\theta_c = -2\varphi'' + 2k\pi. \quad (46)$$

From the analysis in Sec. IV, we have that the period-1 orbits $\{1, k\}(k \in \mathbb{N})$ have

$$\widetilde{v}_{z''}^* = \frac{\exp[2\alpha'(k\pi - \varphi'')] - 1}{\exp[2\alpha'(k\pi - \varphi'')] + 1}. \quad (47)$$

Given a value of φ'', the quantity $\widetilde{v}_{z''}^*$ is determined, leading to the initial velocity:

$$\widetilde{v}_0' = \widetilde{v}_0'' = \widetilde{v}_{z''}^* \sqrt{\left(\frac{\tan\theta'}{\sin\varphi''}\right)^2 + 1}. \quad (48)$$

To ensure $\widetilde{v}_0' \leqslant 1$, we have the following constraint on k:

$$k \leqslant \frac{1}{2\pi\alpha'} \ln\left(\frac{\sqrt{\tan^2\theta' + \sin^2\varphi''} + |\sin\varphi''|}{\sqrt{\tan^2\theta' + \sin^2\varphi''} - |\sin\varphi''|}\right) + \frac{\varphi''}{\pi}. \quad (49)$$

The initial scaled velocity in O' is given by

$$\begin{aligned} \widetilde{v}_{z'}^* &= \widetilde{v}_{z''}^*/\cos\theta',\ \widetilde{v}_{y'}^* = 0, \\ \widetilde{v}_{x'}^* &= \widetilde{v}_{x''}^* = -\widetilde{v}_{z''}^* \tan\theta'/\tan\varphi''. \end{aligned}$$

In the original reference frame O, the initial scaled velocity $\widetilde{\mathbf{v}}_0^*$ associated with the period-1 orbit is

$$\begin{aligned} \widetilde{v}_x^* &= \frac{\widetilde{v}_{x'}^* - \widetilde{v}}{1 - \widetilde{v}_{x'}^* \widetilde{v}}, \\ \widetilde{v}_y^* &= 0, \\ \widetilde{v}_z^* &= \frac{\widetilde{v}_{z'}^*}{\gamma_{\widetilde{v}}(1 - \widetilde{v}_{x'}^* \widetilde{v})}, \end{aligned} \quad (50)$$

where $\gamma_0' \equiv (1 - \widetilde{v}_0'^2)^{-1/2}$ and

$$\gamma_0 = \gamma_0' \gamma_{\widetilde{v}} (1 - \widetilde{v}_{x'}^* \widetilde{v}).$$

The period is given by

$$T_{\{1,k\}} = 2\widetilde{v}_{z''}^*/\gamma_{\widetilde{v}}\omega_0'\alpha' \quad (51)$$

with $\omega_0' = eB'/m\gamma_0'$. The fixed point is located on the curve $\widetilde{v}_y = 0$ on the Poincaré surface of section.

B. Stability of period-1 orbits

The stability of a periodic orbit can be determined by linearizing the Poincaré map about its location [2,26]. linearized Poincaré map is described by a 2×2 monodromy matrix [61], denoted as M, whose elements represent the variation of $\mathcal{V}_{x(y)}$ with respect to $\widetilde{v}_{x(y)}$. The absolute value of the trace $\mathrm{Tr}[M]$ of the matrix M characterizes the stability of the periodic orbit. In particular, if $|\mathrm{Tr}[M]| < 2$, the roots of M are complex and of magnitude one, so the periodic orbit is *elliptic* (stable). In this case, a nearby orbit remains nearby forever in the linear approximation. If $\mathrm{Tr}[M] > 2$ or < -2, the roots are real and positive or negative, and the periodic orbit is *hyperbolic* or *hyperbolic with refection* (unstable), causing nearby orbits to diverge exponentially from the periodic orbit. For $\mathrm{Tr}[M] = 2$, a saddle-node bifurcation occurs, where a stable-unstable pair is created. At the bifurcation, the periodic orbit is marginally stable. As the parameter increases from the bifurcation point, one orbit remains stable in a finite parameter interval, while the other is unstable. For $\mathrm{Tr}[M] = -2$, a period doubling or inverse period doubling bifurcation occurs.

For period-1 orbits, we analytically calculate the monodromy matrix (Appendix A), whose trace is

$$\mathrm{Tr}[M] = (\partial\mathcal{V}_x/\partial\widetilde{v}_x + \partial\mathcal{V}_y/\partial\widetilde{v}_y)_{\widetilde{\mathbf{v}}_0^*} \quad (52)$$

$$\begin{aligned} &= \sin^2(2\theta')\frac{\sinh(\alpha'\xi^*)}{2} \\ &\quad \times \left[\frac{\alpha'\sin\xi^*}{\cosh(\alpha'\xi^*) - 1} + \frac{1}{\alpha'\tan(\xi^*/2)}\right] - \sin^2(2\theta') \\ &\quad + 2[\cos^4\theta'\cos\xi^* + \sin^4\theta'\cosh(\alpha'\xi^*)], \end{aligned} \quad (53)$$

where ξ^* is the motion parameter for period-1 orbits. Without loss of generality, we consider the case $\theta > 0$, so $\partial\alpha'/\partial\alpha > 0$, $\partial\theta'/\partial\theta > 0$, $\partial\alpha'/\partial\theta < 0$, and $\partial\theta'/\partial\alpha < 0$, indicating α' has positive and negative correlations with α and θ, respectively, in contrast to θ'. For convenience, we denote the periodic orbit $\{n, k\}$ as $(n)^{\pm(k)}$, where "$\pm$" corresponds to an initially stable or unstable periodic orbit, respectively [28]. Given γ_0 and θ, as α decreases, so does α', leading to an increase in the motion time and the cyclotron frequency in the reference frame O''. Note that the maximum value of k may increase, i.e., there can be multiple fixed points with $k \geqslant 1$.

Figure 6(a) shows that, as $1/\alpha$ increases, the transcendental equation

$$\gamma_0'(\Delta\theta_c)[1 - \widetilde{v}_{x'}^*(\Delta\theta_c)\widetilde{v}] = \gamma_0/\gamma_{\widetilde{v}}$$

will have a pair of new positive real roots that correspond to the paired period-1 orbits $(1)^{+(k)}$ and $(1)^{-(k)}$ $(k > 0)$ with a saddle-node bifurcation. The $(1)^{-(k)}$ orbit becomes more unstable as $1/\alpha$ increases, until $\mathrm{Tr}[M] \to +\infty$. The other orbit $(1)^{+(k)}$ is stable over a finite interval of the dynamic parameter, until $\mathrm{Tr}[M]$ crosses -2 and tends to $-\infty$. For each $(1)^{+(k)}$ orbit, there is a critical angle $\theta^\dagger$ that depends on the parameters γ_0 and α. For $\theta < \theta^\dagger$, $\mathrm{Tr}[M]$ crosses -2 thrice before approaching asymptotically $-\infty$, as shown in Fig. 6(a). During the process, the $(1)^{+(k)}$ orbit undergoes a period doubling bifurcation, an inverse period doubling bifurcation, and a period doubling bifurcation, respectively, and the third intersection with -2 approaches the second one as θ

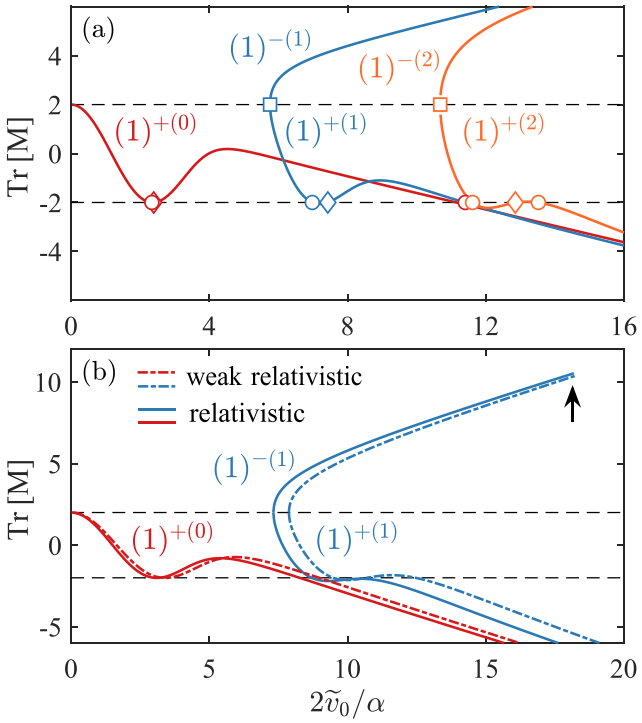

FIG. 6. Trace of the monodromy matrix for period-1 orbits. (a) The trace versus $2\widetilde{v}_0/\alpha$ for $(1)^{+(0)}$ and $(1)^{\pm(k)}$ $(k = 1, 2)$, $\widetilde{v}_0 = 0.8$, and $\theta = \pi/18$. The hollow cycles, diamonds, and squares represent the period doubling bifurcation, inverse period doubling bifurcation, and saddle-node bifurcation, respectively. (b) The trace of as a function of $2\widetilde{v}_0/\alpha$ for $(1)^{+(0)}$ and $(1)^{\pm(1)}$ at $\theta = 16°$, in the relativistic ($\widetilde{v}_0 = 0.5$, solid lines) and weak relativistic ($\widetilde{v}_0 = 0.0005$, chain-dotted lines) regimes, where the black arrow indicates the truncation of the $(1)^{-(1)}$ orbits.

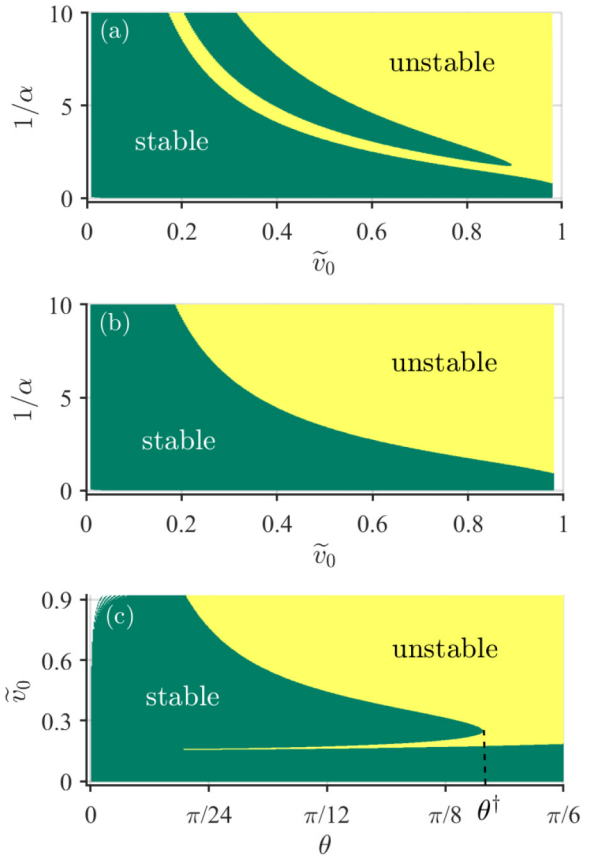

FIG. 7. Stability regions of period-1 orbits. Shown are the stable (green) and unstable (yellow) regions of the $(1)^{+(0)}$ orbit in the plane $(\widetilde{v}_0, 1/\alpha)$ for (a) $\theta = \pi/8$ and (b) $\theta = \pi/6$. (c) The stability regions in the plane $(\theta, \widetilde{v}_0)$ for $1/\alpha = 10$.

increases. For $\theta = \theta^\dagger$, the third intersection with -2 is merged into the second one, so Tr$[M]$ crosses -2 twice, and $(1)^{+(k)}$ no longer goes through the process of re-stabilization. For $\theta > \theta^\dagger$, Tr$[M]$ only crosses -2 once, as shown in Figs. 6(a) and 6(b), corresponding to $\theta = \pi/8 < \theta^\dagger$ and $\theta = \pi/6 > \theta^\dagger$, respectively. Figure 6(b) shows that, for $\theta < \theta^\dagger \approx 4\pi/29$, as $2\widetilde{v}_0/\alpha$ increases, the $(1)^{+(0)}$ orbit is stable at first, becomes unstable, and then becomes stable and unstable again for the given θ value ($< \theta^\dagger$).

Figure 6(b) shows that the $(1)^{-(1)}$ orbits are truncated at the black arrow in both the relativistic and weakly relativistic regimes. In fact, the $(1)^{-(1)}$ and $(1)^{-(2)}$ orbits are also truncated for a sufficiently large value of $2\widetilde{v}_0/\alpha$ [not shown in Fig. 6(a)], where $\alpha^-_{1,k}$ for $(1)^{-(k)}$ $(k > 0)$ denotes the truncation threshold. As will be discussed, the physical reason underlying the truncation is that the elastic collision occurs before a whole self-retracing process. We note that this truncation process was not treated in the previous work [28], which could lead to some spurious periodic orbits when $\beta_{\rm NR}$ is relatively large. In fact, the truncation occurs in the single-barrier dynamics for $(n)^{-(k)}$ in the weakly relativistic regime that degenerates into the nonrelativistic regime smoothly, as shown in Fig. 6(b).

What are the possible effects of special relativity on the period-1 orbits and their stability? In Fig. 6(b), the traces of the monodromy matrix as a function of $2\widetilde{v}_0/\alpha$ for period-1 orbits have a similar behavior in the relativistic and weakly relativistic regimes. In fact, the behavior in the weakly relativistic regime is similar to that in the nonrelativistic regime with approximately the same trace for the same value of $2\widetilde{v}_0/\alpha$. This indicates that special relativity has no significant effect on the period-1 orbits. It is also worth noting that the dynamics in the nonrelativistic regime are determined by two parameters (θ and $\beta_{\rm NR}$) while the dynamics in the relativistic regime are determined by three parameters (θ, $\widetilde{v}_0$, and α). For fixed $2\widetilde{v}_0/\alpha$, $\widetilde{v}_0$ is a dynamic parameter that represents the degree of the special relativity effects. In fact, the dynamic parameter $\beta_{\rm NR}$ contains two components: $\widetilde{v}_0$ and $1/\alpha$, where $\widetilde{v}_0$ is related to the degree of the relativity effects. The connection between the relativistic and nonrelativistic regimes in terms of the stability of the period-1 orbits can be concretely seen in Fig. 7, where the stable and unstable regions for period-1 orbits in the parameter plane are displayed. For $\beta_{\rm NR} = 2\widetilde{v}_0/\alpha$, the behaviors are similar in the weakly relativistic and nonrelativistic regimes, and the $\widetilde{v}_0$ plays a role similar to that of $1/\alpha$.

VI. DISCUSSION

The emergence of chaotic behaviors in nonrelativistic Hamiltonian systems was a subject of study in nonlinear

physics [26,62–67], and there has been a continuous interest in chaos in relativistic systems as well [12–25]. We carried out a fairly complete analysis of the motion of a relativistic charged particle in a potential well generated by two potential barriers in the presence of static electrical and magnetic fields. Depending on the parameters, two types of distinct motion can arise: particles experiencing collisions with a single barrier or both barriers. In both cases, utilizing a specially designed Lorentz boost transform, we were able to derive the Poincaré map for both types of particle motion. Examination of the phase-space structure on the Poincaré surface of section reveals that, as the degree of special relativity effects increases, chaos becomes more extensive, verifying the previously uncovered, pure numerical phenomenon that relativity enhances chaos. A key feature of our work lies in its semianalytic nature: we managed to derive explicit Poincaré maps and the phase-space dynamics that were obtained simply by iterating the maps, in contrast to previous works in which the approach was to numerically solve the Hamilton's equations of motion. For both types of particle motion, we were also able to analytically calculate the periodic orbits of short periods. The analytic approach enables the physical origin of the periodic orbits to be elucidated. We emphasize that in the field of nonlinear dynamics and chaos, analytically solvable models are rare, particularly continuous-time models in Hamiltonian systems. Our success with such a model in relativistic particle dynamics leads to unique insights into the physics of the dynamical behaviors in terms of the Poincaré map, phase-space structures, chaos, and periodic orbits.

ACKNOWLEDGMENTS

The work at Lanzhou University was supported by National Key R&D Program of China under Grant No. 2023YFA1407101 and by NSFC under Grants No. 12105125, No. 12175090, No. 11775101, and No. 12247101. The work at Arizona State University was supported by the Air Force Office of Scientific Research under Grant No. FA9550-21-1-0438.

APPENDIX A: MONODROMY MATRIX FOR PERIOD-1 ORBITS FOR SINGLE-BARRIER DYNAMICS

We derive the monodromy matrix and its trace period-1 orbits from single-barrier dynamics by examining the behavior of orbits near $\widetilde{\mathbf{v}}_0^* = (\widetilde{v}_x^*, \widetilde{v}_y^*, \widetilde{v}_z^*)$. The Poincaré map is two-dimensional with the dynamical variables $\widetilde{v}_x$ and $\widetilde{v}_y$ including $\mathcal{V}_x$ and $\mathcal{V}_y$. Setting

$$\widetilde{v}_x(\xi) = \widetilde{v}_x^* + \delta\widetilde{v}_x(\xi),\ \widetilde{v}_y(\xi) = \widetilde{v}_y^* + \delta\widetilde{v}_y(\xi), \tag{A1}$$

where $\delta\widetilde{v}_x(\xi)$ and $\delta\widetilde{v}_y(\xi)$ are infinitesimal, we expand $\mathcal{V}_x$ and $\mathcal{V}_y$ to the first order of $\delta\widetilde{v}_x(\xi)$ and $\delta\widetilde{v}_y(\xi)$:

$$\mathcal{V}_{x(y)}(\widetilde{v}_x^* + \delta\widetilde{v}_x, \widetilde{v}_y^* + \delta\widetilde{v}_y) = \widetilde{v}_{x(y)}^* + \frac{\partial\mathcal{V}_{x(y)}}{\partial\widetilde{v}_x}\delta\widetilde{v}_x + \frac{\partial\mathcal{V}_{x(y)}}{\partial\widetilde{v}_y}\delta\widetilde{v}_y + O((\delta\widetilde{v}_x)^2, (\delta\widetilde{v}_y)^2, \delta\widetilde{v}_x\delta\widetilde{v}_y), \tag{A2}$$

and $M = (M)_{ij}$ is the Jacobian matrix of partial derivatives of the Poincaré map,

$$M = \begin{pmatrix} \partial\mathcal{V}_x/\partial\widetilde{v}_x & \partial\mathcal{V}_x/\partial\widetilde{v}_y \\ \partial\mathcal{V}_y/\partial\widetilde{v}_x & \partial\mathcal{V}_y/\partial\widetilde{v}_y \end{pmatrix}. \tag{A3}$$

The trace of M is

$$\begin{aligned} \mathrm{Tr}[M] &= (\partial\mathcal{V}_x/\partial\widetilde{v}_x + \partial\mathcal{V}_y/\partial\widetilde{v}_y)_{\widetilde{\mathbf{v}}_0^*} \\ &= \gamma_{\tilde{v}}^2(1+\widetilde{v}_x^*\widetilde{v})^2\left(\frac{\partial\widetilde{v}_{x''}(\xi)}{\partial\widetilde{v}_x}\right)_{\widetilde{\mathbf{v}}_0^*} + \gamma_{\tilde{v}}(1+\widetilde{v}_x^*\widetilde{v})\left[\cos\theta'\left(\frac{\partial\widetilde{v}_{y''}(\xi)}{\partial\widetilde{v}_y}\right)_{\widetilde{\mathbf{v}}_0^*} + \sin\theta'\left(\frac{\partial\widetilde{v}_{z''}(\xi)}{\partial\widetilde{v}_y}\right)_{\widetilde{\mathbf{v}}_0^*}\right]. \end{aligned} \tag{A4}$$

The period-1 orbits are denoted by $\{1, k\}$ satisfy $2k\pi < \xi_0 = \xi^* = \Delta\theta_c < 2(k+1)\pi$, where $\Delta\theta_c$ is the positive real root of the equation

$$\gamma_0'(\Delta\theta_c)[1 - \widetilde{v}_{x'}^*(\Delta\theta_c)\widetilde{v}] = \gamma_0/\gamma_{\tilde{v}}$$

with the precondition $\widetilde{v}_0' \leqslant 1$. We get

$$\begin{aligned} \left(\frac{\partial\widetilde{v}_{z''}(\xi)}{\partial\widetilde{v}_y}\right)_{\widetilde{\mathbf{v}}_0^*} &= \left(\frac{\partial\widetilde{v}_{z''}}{\partial\widetilde{v}_y}\right)_{\widetilde{\mathbf{v}}_0^*} + \left(\frac{\partial\xi}{\partial\widetilde{v}_y}\right)_{\widetilde{\mathbf{v}}_0^*}\alpha'(\widetilde{v}_{z''}^{*2} - 1), \\ \left(\frac{\partial\widetilde{v}_{y''}(\xi)}{\partial\widetilde{v}_y}\right)_{\widetilde{\mathbf{v}}_0^*} &= \left(\frac{\partial\widetilde{v}_{y''}}{\partial\widetilde{v}_y}\right)_{\widetilde{\mathbf{v}}_0^*}\cos\xi^* - \left(\frac{\partial\widetilde{v}_{z''}}{\partial\widetilde{v}_y}\right)_{\widetilde{\mathbf{v}}_0^*}\widetilde{v}_{y''}^*\sinh(\alpha'\xi^*) + \left(\frac{\partial\xi}{\partial\widetilde{v}_y}\right)_{\widetilde{\mathbf{v}}_0^*}(\widetilde{v}_{x''}^* + \alpha'\widetilde{v}_{y''}^*\widetilde{v}_{z''}^*), \\ \left(\frac{\partial\widetilde{v}_{x''}(\xi)}{\partial\widetilde{v}_x}\right)_{\widetilde{\mathbf{v}}_0^*} &= \left(\frac{\partial\widetilde{v}_{x''}}{\partial\widetilde{v}_x}\right)_{\widetilde{\mathbf{v}}_0^*}\cos\xi^* - \left(\frac{\partial\widetilde{v}_{y''}}{\partial\widetilde{v}_x}\right)_{\widetilde{\mathbf{v}}_0^*}\sin\xi^* + \left(\frac{\partial\widetilde{v}_{z''}}{\partial\widetilde{v}_x}\right)_{\widetilde{\mathbf{v}}_0^*}\widetilde{v}_{x''}^*\sinh(\alpha'\xi^*) + \left(\frac{\partial\xi}{\partial\widetilde{v}_x}\right)_{\widetilde{\mathbf{v}}_0^*}(\widetilde{v}_{y''}^* - \alpha'\widetilde{v}_{x''}^*\widetilde{v}_{z''}^*). \end{aligned} \tag{A5}$$

Let ξ be the root of $\mathcal{F}(\xi, \widetilde{v}_x, \widetilde{v}_y) = 0$. We have

$$\left(\frac{\partial \xi}{\partial \widetilde{v}_j}\right)_{\widetilde{\mathbf{v}}_0^*} = -\frac{\left(\partial \mathcal{F}/\partial \widetilde{v}_j\right)_{\widetilde{\mathbf{v}}_0^*}}{\left(\partial \mathcal{F}/\partial \xi\right)_{\widetilde{\mathbf{v}}_0^*}} = \frac{\cos^2\theta'}{\alpha' \widetilde{v}_{z''}^*}\left(\frac{\partial \mathcal{F}}{\partial \widetilde{v}_j}\right)_{\widetilde{\mathbf{v}}_0^*}, (j = x, y),$$
$$\left(\frac{\partial \mathcal{F}}{\partial \widetilde{v}_j}\right)_{\widetilde{\mathbf{v}}_0^*} = \left(\frac{\partial \widetilde{v}_{z''}}{\partial \widetilde{v}_j}\right)_{\widetilde{\mathbf{v}}_0^*} \sinh(\alpha' \xi^*) - \alpha' \tan\theta' \left[\left(\frac{\partial \widetilde{v}_{y''}}{\partial \widetilde{v}_j}\right)_{\widetilde{\mathbf{v}}_0^*} \sin\xi^* + \left(\frac{\partial \widetilde{v}_{x''}}{\partial \widetilde{v}_j}\right)_{\widetilde{\mathbf{v}}_0^*} (1 - \cos\xi^*)\right]. \tag{A6}$$

The partial derivatives of the fixed point are

$$\left(\frac{\partial \widetilde{v}_{x''}}{\partial \widetilde{v}_x}\right)_{\widetilde{\mathbf{v}}_0^*} = \frac{1}{\gamma_{\widetilde{v}}^2 (1 + \widetilde{v}_x^* \widetilde{v})^2}, \left(\frac{\partial \widetilde{v}_{y''}}{\partial \widetilde{v}_x}\right)_{\widetilde{\mathbf{v}}_0^*} = \frac{(\widetilde{v}_x^* + \widetilde{v}_0^2 \widetilde{v}) \sin\theta'}{\gamma_{\widetilde{v}} \widetilde{v}_z^* (1 + \widetilde{v}_x^* \widetilde{v})^2}, \left(\frac{\partial \widetilde{v}_{z''}}{\partial \widetilde{v}_x}\right)_{\widetilde{\mathbf{v}}_0^*} = -\frac{(\widetilde{v}_x^* + \widetilde{v}_0^2 \widetilde{v}) \cos\theta'}{\gamma_{\widetilde{v}} \widetilde{v}_z^* (1 + \widetilde{v}_x^* \widetilde{v})^2},$$
$$\left(\frac{\partial \widetilde{v}_{x''}}{\partial \widetilde{v}_y}\right)_{\widetilde{\mathbf{v}}_0^*} = 0, \left(\frac{\partial \widetilde{v}_{y''}}{\partial \widetilde{v}_y}\right)_{\widetilde{\mathbf{v}}_0^*} = \frac{\cos\theta'}{\gamma_{\widetilde{v}} (1 + \widetilde{v}_x^* \widetilde{v})}, \left(\frac{\partial \widetilde{v}_{z''}}{\partial \widetilde{v}_y}\right)_{\widetilde{\mathbf{v}}_0^*} = \frac{\sin\theta'}{\gamma_{\widetilde{v}} (1 + \widetilde{v}_x^* \widetilde{v})}. \tag{A7}$$

Substituting the expressions (A5) ∼ (A7) into Eq. (A4), we get

$$\mathrm{Tr}[M] = \sin^2(2\theta') \frac{\sinh(\alpha' \xi^*)}{2}\left[\frac{\alpha' \sin\xi^*}{\cosh(\alpha' \xi^*) - 1} + \frac{1}{\alpha' \tan(\xi^*/2)}\right] + 2[\cos^4\theta' \cos\xi^* + \sin^4\theta' \cosh(\alpha' \xi^*)] - \sin^2(2\theta'). \tag{A8}$$

MONODROMY MATRIX FOR PERIOD-N ORBITS FROM DOUBLE-BARRIER DYNAMICS

A period-n orbit with s elastic collisions (including those with the left and right barriers) will experience s encounters with Poincaré section, where $n \leqslant s \leqslant 2n$. Donating M_k as the monodromy matrix of the kth Poincaré mapping, which is deduced in a similar way as the monodromy matrix for period-1 orbits in the single-barrier dynamics. The only change is to replace the initial scaled velocity $\widetilde{\mathbf{v}}_0$ and motion parameter ξ_* by $\widetilde{\mathbf{v}}_k''$ and ξ_k, respectively, which represent the scaled velocity in O at the moment after the kth elastic collision and the motion parameter for the kth integrable path. We get

$$\begin{aligned}(M_k)_{1j} &= \frac{[1 + (\widetilde{v}_x)_{k+1} \widetilde{v}]^2}{1 - \widetilde{v}^2}\left(\frac{\partial \widetilde{v}_{x''}(\xi_{k+1})}{\partial \widetilde{v}_j}\right)_{\widetilde{\mathbf{v}}_k} \\ &= \frac{\gamma_0''[1 + (\widetilde{v}_x)_{k+1} \widetilde{v}]^2}{\gamma''(\xi_{k+1})(1 - \widetilde{v}^2)}\left\{\left(\frac{\partial \widetilde{v}_{x''}}{\partial \widetilde{v}_j}\right)_{\widetilde{\mathbf{v}}_k} [\cos\xi_{k+1}(f_k + 1) - f_k] - \left(\frac{\partial \widetilde{v}_{y''}}{\partial \widetilde{v}_j}\right)_{\widetilde{\mathbf{v}}_k} \sin\xi_{k+1}(f_k + 1) + \left(\frac{\partial \widetilde{v}_{z''}}{\partial \widetilde{v}_j}\right)_{\widetilde{\mathbf{v}}_k} g_k\right\},\end{aligned} \tag{B1}$$

where

$$\begin{aligned} f_k &= -[\widetilde{v}_{y''}(\xi_{k+1}) - \alpha' \widetilde{v}_{x''}(\xi_{k+1}) \widetilde{v}_{z''}(\xi_{k+1})] \big/ [\cot\theta' (\widetilde{v}_{z''})_{k+1} - (\widetilde{v}_{y''})_{k+1}], \\ g_k &= \sinh(\alpha' \xi_{k+1})[\widetilde{v}_{x''}(\xi_{k+1}) + f_k/\alpha' \tan\theta'], \\ \gamma_0''/\gamma''(\xi_{k+1}) &= [\cosh(\alpha' \xi_{k+1}) - \sinh(\alpha' \xi_{k+1})(\widetilde{v}_{z''})_k]^{-1}. \end{aligned} \tag{B2}$$

We also have

$$\begin{aligned}(M_k)_{2j} &= \gamma_{\widetilde{v}}[1 + (\widetilde{v}_x)_{k+1} \widetilde{v}]\left[\cos\theta'\left(\frac{\partial \widetilde{v}_{y''}(\xi_{k+1})}{\partial \widetilde{v}_j}\right)_{\widetilde{\mathbf{v}}_k} + \sin\theta'\left(\frac{\partial \widetilde{v}_{z''}(\xi_{k+1})}{\partial \widetilde{v}_j}\right)_{\widetilde{\mathbf{v}}_k}\right] + \frac{(\widetilde{v}_y)_{k+1} \widetilde{v}}{1 + (\widetilde{v}_x)_{k+1} \widetilde{v}}(M_k)_{1j} \\ &= \frac{(\widetilde{v}_y)_{k+1} \widetilde{v}}{1 + (\widetilde{v}_x)_{k+1} \widetilde{v}}(M_k)_{1j} + \gamma_{\widetilde{v}}[1 + (\widetilde{v}_x)_{k+1} \widetilde{v}] \frac{\gamma_0''}{\gamma''(\xi_{k+1})}\left\{\left(\frac{\partial \widetilde{v}_{x''}}{\partial \widetilde{v}_j}\right)_{\widetilde{\mathbf{v}}_k} [\cos\theta' \sin\xi_{k+1} + l_k(\cos\xi_{k+1} - 1)]\right. \\ &\quad \left. + \left(\frac{\partial \widetilde{v}_{y''}}{\partial \widetilde{v}_j}\right)_{\widetilde{\mathbf{v}}_k} (\cos\theta' \cos\xi_{k+1} - l_k \sin\xi_{k+1}) + \left(\frac{\partial \widetilde{v}_{z''}}{\partial \widetilde{v}_j}\right)_{\widetilde{\mathbf{v}}_k}\left[m_k + \sin\theta' \frac{\gamma_0''}{\gamma''(\xi_{k+1})}\right]\right\},\end{aligned} \tag{B3}$$

where

$$\begin{aligned} l_k &= \left\{[\widetilde{v}_{x''}(\xi_{k+1}) + \alpha' \widetilde{v}_{y''}(\xi_{k+1}) \widetilde{v}_{z''}(\xi_{k+1})] \cos\theta' + \alpha' \sin\theta' \left[\widetilde{v}_{z''}^2(\xi_{k+1}) - 1\right]\right\} \big/ [\cot\theta' (\widetilde{v}_{z''})_{k+1} - (\widetilde{v}_{y''})_{k+1}], \\ m_k &= \sinh(\alpha' \xi_{k+1})[\cos\theta' \widetilde{v}_{y''}(\xi_{k+1}) + l_k/\alpha' \tan\theta']. \end{aligned} \tag{B4}$$

In terms of the map $\boldsymbol{\mathcal{V}}''$, we have

$$\begin{aligned}
\widetilde{v}_{x''}(\xi_{k+1}) &= (\widetilde{v}_{x''})_{k+1},\\
\widetilde{v}_{y''}(\xi_{k+1}) &= \cos 2\theta'(\widetilde{v}_{y''})_{k+1} + \sin 2\theta'(\widetilde{v}_{z''})_{k+1},\\
\widetilde{v}_{z''}(\xi_{k+1}) &= \sin 2\theta'(\widetilde{v}_{y''})_{k+1} - \cos 2\theta'(\widetilde{v}_{z''})_{k+1},
\end{aligned} \tag{B5}$$

with the partial derivatives given by

$$\begin{aligned}
\left(\frac{\partial\widetilde{v}_{x''}}{\partial\widetilde{v}_x}\right)_{\widetilde{\mathbf{v}}_k} &= \frac{1}{\gamma_{\widetilde{v}}^2[1+(\widetilde{v}_x)_k\widetilde{v}]^2}, \left(\frac{\partial\widetilde{v}_{x''}}{\partial\widetilde{v}_y}\right)_{\widetilde{\mathbf{v}}_k} = 0,\\
\left(\frac{\partial\widetilde{v}_{y''}}{\partial\widetilde{v}_x}\right)_{\widetilde{\mathbf{v}}_k} &= \frac{\left[(\widetilde{v}_x)_k+\widetilde{v}_0^2\widetilde{v}\right]\sin\theta' - (\widetilde{v}_y)_k\widetilde{v}[(\widetilde{v}_y)_k\sin\theta' + (\widetilde{v}_z)_k\cos\theta']}{\gamma_{\widetilde{v}}(\widetilde{v}_z)_k[1+(\widetilde{v}_x)_k\widetilde{v}]^2},\\
\left(\frac{\partial\widetilde{v}_{z''}}{\partial\widetilde{v}_x}\right)_{\widetilde{\mathbf{v}}_k} &= -\frac{\left[(\widetilde{v}_x)_k+\widetilde{v}_0^2\widetilde{v}\right]\cos\theta' + (\widetilde{v}_y)_k\widetilde{v}[(\widetilde{v}_z)_k\sin\theta' - (\widetilde{v}_y)_k\cos\theta']}{\gamma_{\widetilde{v}}(\widetilde{v}_z)_k[1+(\widetilde{v}_x)_k\widetilde{v}]^2},\\
\left(\frac{\partial\widetilde{v}_{y''}}{\partial\widetilde{v}_y}\right)_{\widetilde{\mathbf{v}}_k} &= \frac{(\widetilde{v}_y)_k\sin\theta' + (\widetilde{v}_z)_k\cos\theta'}{\gamma_{\widetilde{v}}(\widetilde{v}_z)_k[1+(\widetilde{v}_x)_k\widetilde{v}]}, \left(\frac{\partial\widetilde{v}_{z''}}{\partial\widetilde{v}_y}\right)_{\widetilde{\mathbf{v}}_k} = \frac{(\widetilde{v}_z)_k\sin\theta' - (\widetilde{v}_y)_k\cos\theta'}{\gamma_{\widetilde{v}}(\widetilde{v}_z)_k[1+(\widetilde{v}_x)_k\widetilde{v}]}.
\end{aligned} \tag{B6}$$

The quantities $\widetilde{\mathbf{v}}_k$ and ξ_k can be numerically calculated according to the quantitative description of period-n orbits. The matrix $(M_k)_{ij}$ can be obtained by using Eqs. (B1) and (B3).

APPENDIX C: PERIOD-2 ORBITS FROM SINGLE-BARRIER DYNAMICS

In the single-barrier dynamics regime, our analysis reveals two types of periodic orbits of period-2, with distinct physical origin and stability, in terms of whether there is "mixing" in the reference frame O''. In particular, for a nonmixing orbit, there is no energy exchange between the longitudinal and cyclotron motion components after each elastic collision with the left barrier. In the following, the two types of period-2 orbits are treated separately.

1. Type A: nonmixing period-2 orbits

After an elastic collision, the direction of $\widetilde{v}_{z''}$ of the orbit is reversed and its magnitude may change as governed by

$$\widetilde{v}_{z''}(\xi_1^+) = -\widetilde{v}_{z''}(\xi_1^-),$$

which indicates that the component of the velocity in the (y'', z'') plane is perpendicular to the left barrier immediately before the collision. It also means that the longitudinal motion is not a whole reentry motion in the process of $\widetilde{v}_{z''} \to 0 \to -\widetilde{v}_{z''}$. As a result, we have

$$\widetilde{v}_{y''}(\xi_1^-) = -\tan\theta'\widetilde{v}_{z''}(\xi_1^-),$$

leading to the following relations for particle motion immediately before and after the first elastic collision:

$$\begin{aligned}
\widetilde{v}_{x''}(\xi_1^+) &= \widetilde{v}_{x''}(\xi_1^-),\\
\widetilde{v}_{y''}(\xi_1^+) &= -\widetilde{v}_{y''}(\xi_1^-),\\
\widetilde{v}_{z''}(\xi_1^+) &= -\widetilde{v}_{z''}(\xi_1^-),
\end{aligned} \tag{C1}$$

where ξ_1 is a parameter characterizing the particle motion in between the collisions.

Since the cyclotron motion has no effect on the longitudinal motion, but the latter can affect the former, we focus on the latter. The first criterion for a periodic orbit is returning to the original position: $z''(\xi_1+\xi_2) = 0$, which requires that the longitudinal scaled velocity goes through the following process:

$$\widetilde{v}_{z''} \xrightarrow{\text{1IP}} \widetilde{v}_{z''}(\xi_1^-) \xrightarrow{\text{1EC}} -\widetilde{v}_{z''}(\xi_1^-) \xrightarrow{\text{2IP}} -\widetilde{v}_{z''}, \tag{C2}$$

which is equivalent to the motion cutting off a segment of $\widetilde{v}_{z''}(\xi_1^-) \to 0 \to -\widetilde{v}_{z''}(\xi_1^-)$ on a whole reentry motion if $\widetilde{v}_{z''}(\xi_1^-) > 0$, or the motion with the added segment of $-\widetilde{v}_{z''}(\xi_1^-) \to 0 \to \widetilde{v}_{z''}(\xi_1^-)$ on a whole reentry motion if $\widetilde{v}_{z''}(\xi_1^-) < 0$. The second criterion is the coincidence of the velocity:

$$\widetilde{v}_{z''}(\xi_1+\xi_2) = \widetilde{v}_{z''},$$

requiring $-\widetilde{v}_{z''} \xrightarrow{\text{2EC}} \widetilde{v}_{z''}$ or $\widetilde{v}_{y''} = -\tan\theta'\widetilde{v}_{z''}$. Type A period-2 orbits thus originate from relevant period-1 orbits, degenerating into the $(1)^{+(k)}$ orbits at the first period doubling bifurcation.

The cyclotron motion associated with type-A period-2 orbits can then be analyzed. Since, for longitudinal motion, we have

$$\begin{aligned}
\widetilde{v}_{z''} &\xrightarrow{\text{1IP}} \widetilde{v}_{z''}(\xi_1^-),\\
-\widetilde{v}_{z''}(\xi_1^-) &\xrightarrow{\text{2IP}} -\widetilde{v}_{z''},
\end{aligned}$$

ξ_2 is equal to ξ_1, leading to

$$\begin{aligned}
\widetilde{v}_{y''}(\xi_2^-) &= [\widetilde{v}_{y''}(\xi_1^+)\cos\xi_2 + \widetilde{v}_{x''}(\xi_1^+)\sin\xi_2]\gamma''(\xi_1)/\gamma_0''\\
&= [-\widetilde{v}_{y''}(\xi_1^-)\cos\xi_1 + \widetilde{v}_{x''}(\xi_1^-)\sin\xi_1]\gamma''(\xi_1)/\gamma_0''\\
&= -(\widetilde{v}_{y''}\cos\xi_1 + \widetilde{v}_{x''}\sin\xi_1)\cos\xi_1\\
&\quad + (\widetilde{v}_{x''}\cos\xi_1 - \widetilde{v}_{y''}\sin\xi_1)\sin\xi_1\\
&= -\widetilde{v}_{y''} \xrightarrow{\text{2EC}} \widetilde{v}_{y''}.
\end{aligned} \tag{C3}$$

The equality $\widetilde{v}_{x''}(\xi_2^-) = \widetilde{v}_{x''}$ can be analyzed in the same way. In addition, to ensure returning to the original position for a period-2 orbit, two successive elastic collisions need to satisfy $z''(\xi_{1,2}) - y''(\xi_{1,2})\tan\theta' = 0$.

The condition for type-A period-2 orbits with the initial scaled velocity $\widetilde{\mathbf{v}}''$ to arise is then

$$\widetilde{v}_{y''} = -\tan\theta'\widetilde{v}_{z''},\ \widetilde{v}_{y''}(\xi_1^-) = -\tan\theta'\widetilde{v}_{z''}(\xi_1^-), \tag{C4}$$

with ξ_1 given by Eq. (20). For given γ_0, $\widetilde{v}_{z''}$ can be regarded as an independent variable, and

$$\widetilde{v}_{x''}(\widetilde{v}_{z''}) = \frac{\gamma_{\widetilde{v}}^2\widetilde{v} \pm \gamma_0\sqrt{\gamma_0^2 - \widetilde{v}_{z''}^2\sec^2\theta'\left(\gamma_0^2+\gamma_{\widetilde{v}}^2-1\right)-1}}{\gamma_0^2+\gamma_{\widetilde{v}}^2-1} \tag{C5}$$

can be obtained by solving

$$\gamma_0 = \gamma_0'\gamma_{\widetilde{v}}(1-\widetilde{v}_{x''}\widetilde{v}).$$

The quantity $\mathcal{F}_\pm(\xi,\widetilde{v}_{z''})$ as the function of ξ and $\widetilde{v}_{z''}$ can be obtained by substituting the "±" forms of $\widetilde{v}_{x''}$ into $\mathcal{F}$. Defining an implicit function $\mathcal{S}$ as

$$\begin{aligned}\mathcal{S}(\xi,\widetilde{v}_{z''}) &\equiv [\widetilde{v}_{y''}(\xi_1^-) + \tan\theta'\widetilde{v}_{z''}(\xi_1^-)]\gamma''(\xi_1)/\gamma_0'' \\ &= \tan\theta'\widetilde{v}_{z''}[\cosh(\alpha'\xi)-\cos\xi] \\ &\quad + \widetilde{v}_{x''}(\widetilde{v}_{z''})\sin\xi - \tan\theta'\sinh(\alpha'\xi) \\ &= 0,\end{aligned} \tag{C6}$$

we can obtain $\mathcal{S}_\pm(\xi,\widetilde{v}_{z''})=0$ in the same way. The analysis leads to the following set of equations for finding the type-A period-2 orbits:

$$\begin{cases}\mathcal{F}_+(\xi,\widetilde{v}_{z''})=0\\ \mathcal{S}_+(\xi,\widetilde{v}_{z''})=0\end{cases}\text{ and }\begin{cases}\mathcal{F}_-(\xi,\widetilde{v}_{z''})=0\\ \mathcal{S}_-(\xi,\widetilde{v}_{z''})=0\end{cases}. \tag{C7}$$

The root set $R_{\gamma_0}=\{(\xi_1^*,\widetilde{v}_{z''}^*)\}$ is the union of the solution sets of Eqs. (C7), where ξ_1^* is the first positive real root of equation $\mathcal{F}_\pm(\xi,\widetilde{v}_{z''}^*)=0$.

The initial scaled velocity $(\widetilde{v}_x^*,\widetilde{v}_y^*,\widetilde{v}_z^*)$ can be obtained from R_{γ_0}. We have

$$\widetilde{v}_{z'}^* = \widetilde{v}_{z''}^*/\cos\theta',\ \widetilde{v}_{y'}^*=0,\ \widetilde{v}_{x'}^* = \widetilde{v}_{x''}(\widetilde{v}_{z''}^*) \tag{C8}$$

in the reference frame O' and

$$\begin{aligned}\widetilde{v}_x^* &= \frac{\widetilde{v}_{x'}^*-\widetilde{v}}{1-\widetilde{v}_{x'}^*\widetilde{v}},\\ \widetilde{v}_y^* &= 0,\\ \widetilde{v}_z^* &= \frac{\widetilde{v}_z^{*'}}{\gamma_{\widetilde{v}}(1-\widetilde{v}_{x'}^*\widetilde{v})}\end{aligned} \tag{C9}$$

in the reference frame O, with the period given by

$$T_{\{2,k\}} = \frac{\sinh(\alpha'\xi_1^*)}{\omega_0'\gamma_{\widetilde{v}}\alpha'}\left(2+\left(1-\widetilde{v}_{z''}^{*2}\right)[1-\cosh(\alpha'\xi_1^*)]\right). \tag{C10}$$

It can be seen that not all the type-A period-2 orbits are located on the curve defined by $\widetilde{v}_y=0$ in the Poincaré map.

2. Type B period-2 orbits

We consider the situation where the trajectory of the particle returns to itself in the plane (y'',z'') in the reference frame O'': $y''(\xi_1)=z''(\xi_1)=0$ (not $x''(\xi_1)=0$), where $\mathbf{x}''(0)\equiv 0$ and ξ_1 is the motion parameter given by Eq. (20). For a period-2 orbit, the trajectory touches the left barrier at two points. Setting $y''(\xi_1)=z''(\xi_1)=0$ and substituting Eqs. (C11) into Eqs. (17), we obtain

$$\begin{aligned}\widetilde{v}_{z''} &= \frac{\exp(\alpha'\xi_1)-1}{\exp(\alpha'\xi_1)+1},\\ \widetilde{v}_{y''} &= -\widetilde{v}_{x''}\tan(\xi_1/2),\end{aligned} \tag{C11}$$

and

$$\widetilde{v}_{x''}(\xi_1^-) = \widetilde{v}_{x''},\ \widetilde{v}_{y''}(\xi_1^-) = -\widetilde{v}_{y''},\ \widetilde{v}_{z''}(\xi_1^-) = -\widetilde{v}_{z''}. \tag{C12}$$

For such an orbit, there is an energy change or "mixing" between the longitudinal and cyclotron motions after the first collision with the left carrier, which is given by

$$\begin{aligned}\delta_{\epsilon_L} &= m\gamma_0'c^2|\sin 2\theta'|\sqrt{\widetilde{v}_{y''}^2-\widetilde{v}_{z''}^2-2\widetilde{v}_{y''}\widetilde{v}_{z''}\cot 2\theta'}\\ &\neq 0.\end{aligned} \tag{C13}$$

The energy exchanging process can be intuitively seen in the O' frame. From Eqs. (C12), we have

$$\widetilde{v}_{x'}(\xi_1^-) = \widetilde{v}_{x'},\ \widetilde{v}_{y'}(\xi_1^-) = -\widetilde{v}_{y'},\ \widetilde{v}_{z'}(\xi_1^-) = -\widetilde{v}_{z'}, \tag{C14}$$

after the first collision with the barrier at which $\widetilde{v}_{z'}$ is reversed. Similar behaviors occur for the second collision. For the whole orbit, we have

$$\begin{aligned}(\widetilde{v}_{x'},\widetilde{v}_{y'},\widetilde{v}_{z'}) &\xrightarrow{\text{1IP}} (\widetilde{v}_{x'},-\widetilde{v}_{y'},-\widetilde{v}_{z'}) \xrightarrow{\text{1EC}} (\widetilde{v}_{x'},-\widetilde{v}_{y'},\widetilde{v}_{z'})\\ &\xrightarrow{\text{2IP}} (\widetilde{v}_{x'},\widetilde{v}_{y'},-\widetilde{v}_{z'}) \xrightarrow{\text{2EC}} (\widetilde{v}_{x'},\widetilde{v}_{y'},\widetilde{v}_{z'}),\end{aligned} \tag{C15}$$

where the condition $\widetilde{\mathbf{v}}''(\xi_1+\xi_2)=\widetilde{\mathbf{v}}''$ is met for arbitrary parameter values of ξ_1 and $\widetilde{v}_{x''}$, and ξ_2 is the first positive real root of

$$\mathcal{F}[\xi;\widetilde{\mathbf{v}}''(\xi_1^+)]=0.$$

Such an orbit is then a type-B period-2 orbit insofar as $z''(\xi_1+\xi_2)=y''(\xi_1+\xi_2)=0$, i.e.,

$$\begin{aligned}-\widetilde{v}_{y''}\sin 2\theta' + \widetilde{v}_{z''}\cos 2\theta' &= \frac{\exp(\alpha'\xi_2)-1}{\exp(\alpha'\xi_2)+1},\\ \widetilde{v}_{y''}\cos 2\theta' + \widetilde{v}_{z''}\sin 2\theta' &= \widetilde{v}_{x''}\tan(\xi_2/2),\end{aligned} \tag{C16}$$

which are equivalent to

$$\mathcal{O} = \tan\left[\frac{1}{2\alpha'}\ln\left(\frac{1+\widetilde{v}_{x''}\tan(\xi_1/2)\sin 2\theta'+\widetilde{v}_{z''}\cos 2\theta'}{1-\widetilde{v}_{x''}\tan(\xi_1/2)\sin 2\theta'-\widetilde{v}_{z''}\cos 2\theta'}\right)\right] + \tan(\xi_1/2)\cos 2\theta' - \sin 2\theta'\widetilde{v}_{z''}/\widetilde{v}_{x''} = 0, \tag{C17}$$

after eliminating the motion parameter ξ_2.

When ξ_1 is regarded as an independent variable, $\widetilde{v}_{x''}$ is also a variable and $\widetilde{v}_{z''}(\xi_1)$ is a function of ξ_1, so $\mathcal{O}$ is a function of ξ_1 and $\widetilde{v}_{x''}$. Noting the relation

$$\gamma_0'(\xi_1,\widetilde{v}_x'') = \left[1-\widetilde{v}_x''^2-\widetilde{v}_y''^2(\xi_1,\widetilde{v}_x'')-\widetilde{v}_z''^2(\xi_1)\right]^{-1/2},$$

we have that, if γ_0 is given in the frame O, the constraint for the system is

$$\gamma_0 = \gamma_0'\gamma_{\widetilde{v}}(1 - \widetilde{v}_{x''}\widetilde{v}). \tag{C18}$$

In this case, $\widetilde{v}_{x''}$ as a function of ξ_1 is no longer an independent variable:

$$\widetilde{v}_{x''}(\xi_1) = \left(\gamma_{\widetilde{v}}^2\widetilde{v} \pm \frac{\gamma_0\gamma_{\widetilde{v}}}{\gamma_{\widetilde{v}_{z''}}}\left|\sec\frac{\xi_1}{2}\right|\sqrt{\widetilde{v}^2\cos^2\frac{\xi_1}{2} + \frac{\gamma_0^2}{\gamma_{\widetilde{v}}^2} - \gamma_{\widetilde{v}_{z''}}^2}\right)\Big/\left(\gamma_{\widetilde{v}}^2\widetilde{v}^2 + \gamma_0^2\sec^2\frac{\xi_1}{2}\right), \tag{C19}$$

with $\gamma_{\widetilde{v}_{z''}} \equiv (1 - \widetilde{v}_{z''}^2)^{-1/2}$. Substituting Eqs. (C19) into the transcendental equation $\mathcal{O}_{\pm}(\xi_1) = 0$, we can find its positive real root set $R_{\gamma_0} = \{\xi_1^*\}$ numerically. Sorting them from the smallest to the largest: $R_{\gamma_0} = \{\xi_{11}^*, \xi_{12}^*, \ldots, \xi_{1c}^*\}$, excludes the motion parameter associated with the period-1 orbits.

In the reference frames O' and O, the initial scaled velocities are

$$\begin{aligned}
\widetilde{v}_{z'}^* &= -\widetilde{v}_{y''}^*\sin\theta' + \widetilde{v}_{z''}^*\cos\theta',\\
\widetilde{v}_{y'}^* &= \widetilde{v}_{y''}^*\cos\theta' + \widetilde{v}_{z''}^*\sin\theta',\\
\widetilde{v}_{x'}^* &= \widetilde{v}_{x''}^*,
\end{aligned} \tag{C20}$$

and

$$\begin{aligned}
\widetilde{v}_x^* &= \frac{\widetilde{v}_{x'}^* - \widetilde{v}}{1 - \widetilde{v}_{x'}^*\widetilde{v}},\\
\widetilde{v}_y^* &= \frac{\widetilde{v}_{y'}^*}{\gamma_{\widetilde{v}}(1 - \widetilde{v}_{x'}^*\widetilde{v})},\\
\widetilde{v}_z^* &= \frac{\widetilde{v}_{z'}^*}{\gamma_{\widetilde{v}}(1 - \widetilde{v}_{x'}^*\widetilde{v})},
\end{aligned} \tag{C21}$$

respectively, with the period

$$\begin{aligned}
T_{\{2,k\}} &= 4\widetilde{v}_{z'}^*\cos\theta'/\omega_0'\gamma_{\widetilde{v}}\alpha'\\
&= 4\widetilde{v}_z^*\cos\theta'/(1 + \widetilde{v}_x^*\widetilde{v})\omega_0'\gamma_{\widetilde{v}}^2\alpha'.
\end{aligned}$$

On the Poincaré surface of section, a type-B period-2 orbit has two points: $(\widetilde{v}_x^*, \widetilde{v}_y^*)$ and $(\widetilde{v}_x^*, -\widetilde{v}_y^*)$ that are symmetric about the line $\widetilde{v}_y = 0$. In fact, due to the time inversion symmetry of the system, the Poincaré map is symmetric about this line. In addition, Type B period-2 orbits are self-retracing with $\widetilde{v}_x \propto \eta \propto y$. The physical reasoning gives essentially the same properties of the type-B period-2 orbits as those from mathematical derivation.

3. Physical origin of period-2 orbits

For $\theta = 0$, the period-2 orbits are helical. From the equality $\widetilde{v}_z(\xi_1^+) = \widetilde{v}_z$, we get $\xi_2 = \xi_1 = \Delta\theta_c/2$. Immediately after the first elastic collision with the barrier, the corresponding point on the Poincaré surface of section does not coincide with the initial point, so the phase change for the motion in between the two successive collisions with the barrier is $\Delta\theta_c/2 = \xi_1 = (k + 1/2)2\pi$. For the whole period-2 orbit, the phase change is $\Delta\theta_c = (2k + 1)2\pi$. The period-2 orbits are thus characterized by the parameter k, which are denoted as $\{2, k\}$.

For $\theta \to 0^+$, all resonant tori $\{2, k\}$ are destroyed and replaced by an integer number of pairs of stable-unstable period-2 orbits, which is similar to the destruction of the tori $\{1, k\}$. These surviving period-2 orbit pairs appear through the saddle-node bifurcation, with infinitesimal deviations in the position and period with respect those in the $\theta = 0$ case. Recall from our stability analysis of the period-1 orbits that the orbits $(1)^{+(k)}$ go through the first period-doubling bifurcation, inverse period doubling bifurcation, and the second period doubling bifurcation, respectively, due to $\theta \to 0^+ < \theta^\dagger$. During the process of going through these bifurcations, two stable and one unstable period-2 orbits appear, and a pair of them, denoted as $(2)^{\pm(k)}$, survives from the destruction of the tori $\{2, k\}$ originating from the fist period-doubling bifurcation and an inverse period-doubling bifurcation: they appear within an infinitesimal interval $\Delta\alpha^{-1} \to 0$, created at the same "time" as stipulated by the Poincaré-Birkhoff theorem [26]. Since, for $\theta = 0$, the two intersection points of the resonant torus and the line $\widetilde{v}_y = 0$ both represent a nonmixing orbit, they survive from the case of $\theta \to 0^+$ and deform into a type-A period-2 orbit $(2)^{+(k)}$ continuously. There is one nonmixing orbit for a resonant torus $\{2, k\}$, so the $(2)^{-(k)}$ orbit must be mixing. Note that, for type-B period-2 orbits, the two intersection points of the resonant torus and the line $\widetilde{v}_x = 0$ survive and deform into a type-B period-2 orbit $(2)^{-(k)}$.

It is worth noting that another type of period-2 orbits exist: they are not self-tracing and mixing, implying the existence of two points with different $\widetilde{v}_x$ and $\widetilde{v}_y$ values on the Poincar'e surface of section, which are denoted as type-C period-2 orbits. These orbits possess a reflection symmetry but in a more subtle manner: they require two additional fixed points to restore the symmetry about the line $\widetilde{v}_y = 0$ in the Poincaré surface of section 28. Also note that, a type-A period-2 orbit $(2)^{+(k)}$ leaves two points separated on both sides of the fixed point $\{1, k\}$ in the Poincaré surface of section, located on the line $\widetilde{v}_y = 0$. As $1/\alpha$ increases, the two points gradually move away from the fixed point until they are close to the edge, with the truncation at the threshold as $1/\alpha_{2,k}^+$, as exemplified in Fig. 8, where the threshold $1/\alpha_{2,0}^+ = 6.268$ is shown by red arrows for the $(2)^{+(0)}$ orbit.

When a $(1)^{+(k)}$ orbit goes through the second period doubling bifurcation, it gives rise to a new stable period-2 orbit with no analog in the untitled system, denoted as $(2)^{*(k)}$. The $(2)^{*(k)}$ orbit appears at large $1/\alpha$ values for small θ, where $\alpha \sim \theta$. Further, the second period-doubling bifurcation will merge with the inverse period doubling bifurcation as θ increases to $\theta^\dagger$, and the orbit $(2)^{*(k)}$ will merge with $(2)^{-(k)}$ too. By continuity, the $(2)^{*(k)}$ and $(2)^{-(k)}$ orbits are of the same type: type-B period-2 orbits.

Figure 9(a) shows, for $\theta < \theta^\dagger$, the $(2)^{-(0)}$ and $(2)^{*(0)}$ orbits appear at points A and B, respectively, corresponding to the inverse period-doubling bifurcation and the second period-doubling bifurcation for the $(1)^{+(0)}$ orbit, as shown

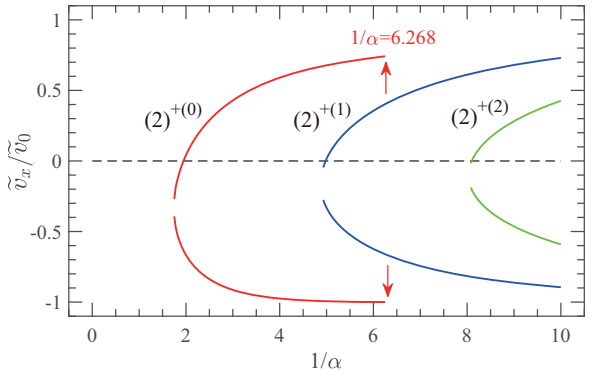

FIG. 8. Bifurcation of type-A period-2 orbits. The orbits are $(2)^{+(k)}$ $(k = 0, 1, 2)$ and the bifurcations occur in the coordinates $(1/\alpha, \widetilde{v}_x/\widetilde{v}_0)$ for $\widetilde{v}_0 = 0.8$ and $\theta = \pi/6$, where the truncation of the $(2)^{+(0)}$ orbit is shown by the red arrow at $1/\alpha^{+}_{2,0} = 6.268$.

in Fig. 6(b). Figure 9(c) shows that, for $\theta > \theta^{\dagger}$, the $(2)^{-(0)}$ and $(2)^{*(0)}$ orbits are no longer produced by inverse period-doubling and the second period-doubling bifurcations as they are no longer possible for the $(1)^{+(0)}$ orbit, as shown in Fig. 6(a)]. The $(2)^{-(0)}$ and $(2)^{*(0)}$ orbits in fact result from a saddle-node bifurcation. When θ is slightly less than $\theta^{\dagger}$, two processes arise. The first is the deformation of the $(2)^{-(0)}$ orbit: As $1/\alpha$ increases, at first this orbit and $(2)^{+(0)}$ appear with a saddle-node bifurcation at point C, then the $(2)^{+(0)}$ orbit is absorbed by $(1)^{+(0)}$ in a backward period-doubling bifurcation, which does not affect the $(2)^{*(0)}$, as shown in Fig. 6(b). The second process is that the backward period-doubling

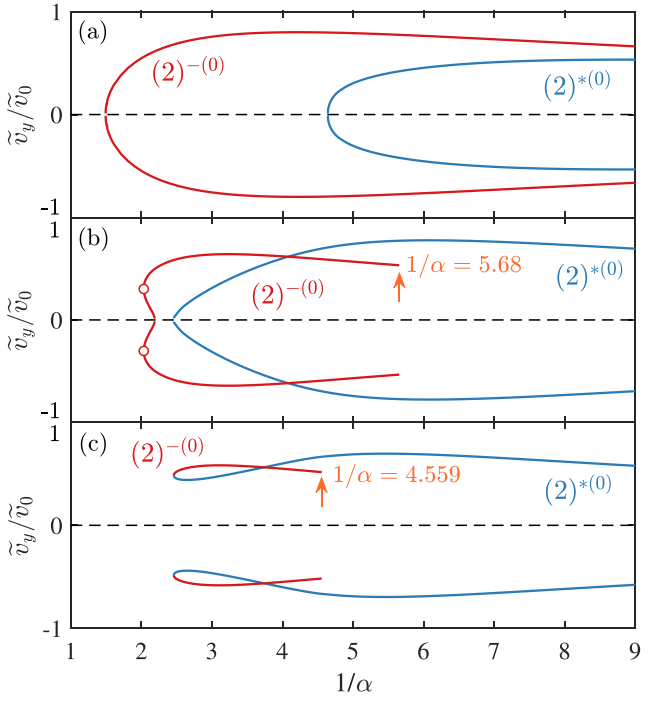

FIG. 9. Bifurcation of type-B period-2 orbits. The orbits are $(2)^{-(0)}$ and $(2)^{*(0)}$ and the bifurcations occur in the coordinates $(1/\alpha, \widetilde{v}_y/\widetilde{v}_0)$ for $\widetilde{v}_0 = 0.8$ and (a) $\theta = \pi/18$, (b) $\theta = \pi/7.7$, and (c) $\theta = \pi/6$.

TABLE I. $\widetilde{\mathbf{v}}''_*$ and ξ^* with different $1/\alpha$ for type A orbits.

$1/\alpha$	$\widetilde{v}^*_{x''}$	$\widetilde{v}^*_{y''}$	$\widetilde{v}^*_{z''}$	ξ^*
4.6	0.5914	−0.2772	0.5032	3.496
5.5	0.6235	−0.2615	0.4681	3.511
6.268	0.6426	−0.2503	0.4447	3.544

bifurcation will merge with the second period-doubling bifurcation and then they disappear together when θ gets closer to $\theta^{\dagger}$ until it exceeds $\theta^{\dagger}$, meaning that the appearance of the $(2)^{-(0)}$ and $(2)^{*(0)}$ orbits is irrelevant to the $(1)^{+(0)}$ orbit, as shown in Fig, 9(c).

The origin and the evolution rule with respect to the dynamic parameter $1/\alpha$ for type-B period-2 orbits shown in Fig. 9 are mostly shared by the dynamics in the nonrelativistic regime, with two differences. First, the $(2)^{-(0)}$ and $(2)^{*(0)}$ orbits intersect at some particular value of $1/\alpha$, at which there is only one type-B period-2 orbit marked by $\{2, 0\}$. This appears to be similar to a transcritical bifurcation [2] but actually it is not such a bifurcation as it is not associated with any stability change. Second, there is a truncation of the $(2)^{-(0)}$ orbit at threshold $1/\alpha^{-}_{2,0}$, as shown in Figs. 9(b) and 9(c).

4. Issue of truncation

As for type-A period-2 orbits, the reason why orbits are cut off is that the first positive real root of $\mathcal{F}(\xi) = 0$ (corresponding to one of the two segments of motion without any elastic collision) is discontinuous at the threshold. Specifically, one of the segments has the motion parameter ξ^*_1 and the other one has ξ^*_2. For $1/\alpha$ below the threshold, the equality $\xi^*_1(=\xi^*_2)$ holds. As $1/\alpha$ crosses the threshold, ξ^*_1 is still continuous but ξ^*_2 is not: $\xi^*_2 \neq \xi^*_1$, violating the requirement for a type-A period-2 orbit. Figure 10(a) shows the motion parameter ξ^*_2 versus $1/\alpha$ with the threshold $1/\alpha = 6.268$. It can be seen that the function $\mathcal{F}(\xi)$ and the curve $\mathcal{F}(\xi) = 0$ are tangent to ξ^* at the threshold

For type-B period-2 orbits, the $(2)^{-(0)}$ orbit is truncated at $1/\alpha^{-}_{2,0}$. Suppose $1/\alpha$ changes in a small interval: $(1/\alpha^{-}_{2,0})^{-} \to (1/\alpha^{-}_{2,0})^{+}$, as exemplified in Fig. 10(b) with $1/\alpha : 4.5 \to 4.6$. The $(2)^{-(0)}$ orbit can then be divided into two segments, each containing a motion in the space and an elastic collision, and each corresponding to a point in the Poincaré surface of section. For $1/\alpha < 1/\alpha^{-}_{2,0}$, the velocity and ξ^* associated with the two segments change continuously. When $1/\alpha$ crosses $1/\alpha^{-}_{2,0}$, the velocity is still continuous but ξ^* is not, as shown in Table II and Fig. 10(b), i.e., the process is no longer self-retracing and the orbit is no longer a period-2 orbit.

We solve the threshold $1/\alpha^{-}_{2,0}$ in terms of the self-retracing process: $z''(\xi_{\rm A}) = y''(\xi_{\rm A}) = 0$, where ξ_A is denoted by the

TABLE II. $\widetilde{\mathbf{v}}''_*$ and ξ^* with different $1/\alpha$ for type B orbits.

$1/\alpha$	$\widetilde{v}^*_{x''}$	$\widetilde{v}^*_{y''}$	$\widetilde{v}^*_{z''}$	ξ^*
4.5	0.6297	0.1652	0.5094	2.605
4.6	0.6366	0.1647	0.5006	5.777

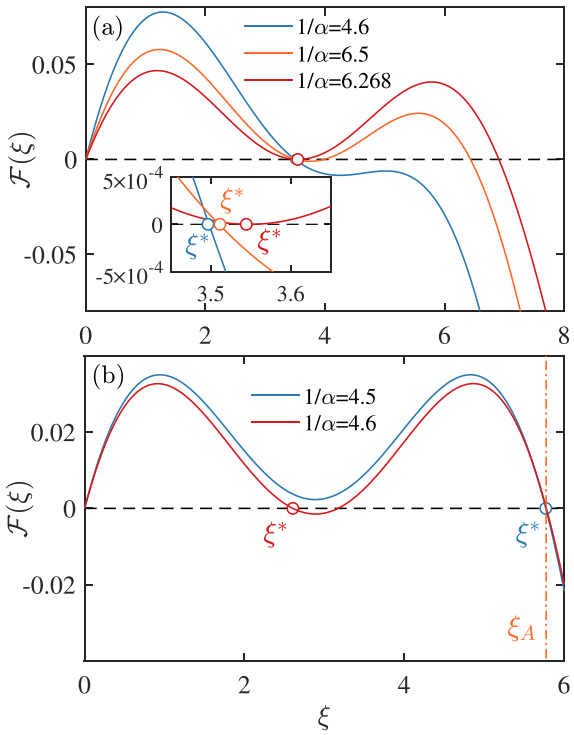

FIG. 10. Motion parameter ξ^* for one of the two motion segments without collision with the barrier. The two values of the two relevant parameters are $\tilde{v}_0 = 0.8$ and $\theta = \pi/6$. (a) For type-A period-2 orbits, $1/\alpha = 4.6$ (blue), $1/\alpha = 5.5$ (orange), $1/\alpha = 6.268$ (red), ξ^* is the first positive real root of the equation $\mathcal{F}(\xi; \tilde{\mathbf{v}}''_*) = 0$, with the value of $\tilde{\mathbf{v}}''_*$ displayed in Table I. (b) For type-B period-2 orbits, $1/\alpha = 4.5$ (blue), $1/\alpha = 4.6$ (red), ξ^* is the first positive real root of $\mathcal{F}(\xi; \tilde{\mathbf{v}}''_*) = 0$, with the values of $\tilde{\mathbf{v}}''_*$ listed in Table II.

vertical dashed-dotted line in Fig. 10(b). The quantity $\tilde{\mathbf{v}}''$ can be represented by ξ_A as

$$\tilde{\mathbf{v}}'' = \left(\tilde{v}_{x''}, -\tilde{v}_{x''} \tan\frac{\xi_A}{2}, \tanh\frac{\alpha'\xi_A}{2}\right), \tag{C22}$$

with an arbitrary $\tilde{v}_{x''}$ representing an arbitrary initial energy with $\tilde{v}_0 \in (0, 1)$. For $\xi \in [0, \xi_A]$, the function $\mathcal{F}(\xi; \tilde{\mathbf{v}}'')$ is symmetric about the line $\xi = \xi_A/2$, as shown in Fig. 10(b). We have

$$\begin{aligned}\delta &\equiv \mathcal{F}\left(\frac{\xi_A}{2} + f; \tilde{\mathbf{v}}''\right) - \mathcal{F}\left(\frac{\xi_A}{2} - f; \tilde{\mathbf{v}}''\right) \\ &= 2\sinh(\alpha' f)\left(\tanh\frac{\alpha'\xi_A}{2}\cosh\frac{\alpha'\xi_A}{2} - \sinh\frac{\alpha'\xi_A}{2}\right) \\ &\quad - 2\alpha'\tan\theta'\tilde{v}_{x''}\sin f\left(\sin\frac{\xi_A}{2} - \tan\frac{\xi_A}{2}\cos\frac{\xi_A}{2}\right) \\ &= 0,\end{aligned} \tag{C23}$$

with an arbitrary real f. The largest positive real root of the equation $\mathcal{F}(\xi_A/2; \tilde{\mathbf{v}}'') = 0$ is $\alpha^-_{2,0}$, where $\xi_A(\alpha)$ is one of the motion parameters for $(2)^{-(0)}$. The value of $\alpha^-_{2,0}$ can be numerically solved by substituting $\tilde{v}_{x''}(\xi_A, \alpha)$, $\alpha'(\alpha)$, and $\theta'(\alpha)$ into $\mathcal{F}(\xi_A/2; \tilde{\mathbf{v}}'') = 0$ with the given $\tilde{v}_0$ and θ values.

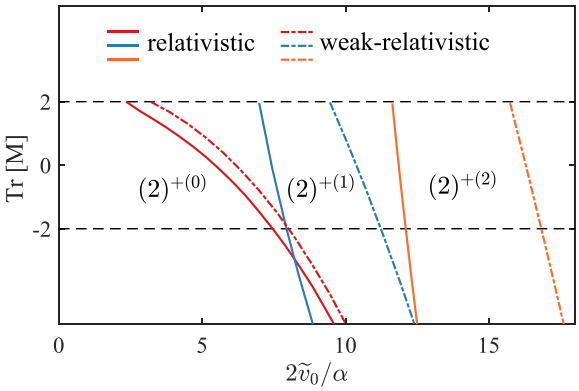

FIG. 11. Trace of the monodromy matrix for type-A period-2 orbits. The orbits are $(2)^{+(k)}$ $(k = 0, 1, 2)$ for $\theta = \pi/18$. The solid and chain-dotted traces correspond to the relativistic regime with $\tilde{v}_0 = 0.8$) and the weakly relativistic regime with $\tilde{v}_0 = 0.008$), respectively.

5. Stability of period-2 orbits

For an period-n orbit in the single-barrier dynamics, the monodromy matrix M is given by $M = \prod_{k=0}^{n-1} M_k$, where M_k is the monodromy matrix of the kth Poincaré mapping, written as

$$(M_k)_{ij} = \left.\frac{\partial \mathcal{V}_i}{\partial \tilde{v}_j}\right|_{\tilde{\mathbf{v}}=\tilde{\mathbf{v}}_k}, \quad (i, j = 1, 2), \tag{C24}$$

with $i, j = 1 \equiv x$ and $i, j = 2 \equiv y$. The scaled velocity is $\tilde{\mathbf{v}}_k$ immediately after the kth collision with the barrier in the frame O (with $\tilde{\mathbf{v}}_0$ being the initial scaled velocity). The motion parameter for the kth segment in between two successive collisions is ξ_k. The specific and general forms of $(M_k)_{ij}$ are shown in Eqs. (B1) and (B3) in Appendix B.

Type-A period-2 orbits satisfy the condition $(\tilde{v}_y)_k = 0$ with $k = 0, 1, 2$ and $\xi^*_1 = \xi^*_2$. We can then obtain the values of $(\tilde{v}_{j''})_1 = \tilde{v}_{j''}(\xi^*_1)$ with $j = x, y, z$. The concrete forms of $(\tilde{v}_j)_k$ can also be obtained by the inverse Lorentz transformation $\Lambda^{-1}(\tilde{v})$, and

$$\begin{aligned}(\tilde{v}_{x''})_1 &= (\tilde{v}_{x''})_0, \\ (\tilde{v}_{y''})_1 &= -(\tilde{v}_{y''})_0\cos 2\theta' - (\tilde{v}_{z''})_0\sin 2\theta', \\ (\tilde{v}_{z''})_1 &= -(\tilde{v}_{y''})_0\sin 2\theta' + (\tilde{v}_{z''})_0\cos 2\theta'.\end{aligned} \tag{C25}$$

Since $\tilde{\mathbf{v}}_k$ and $\tilde{\mathbf{v}}''_k$ are functions of ξ^*_1, the quantity $M(\xi^*_1) = M_0(\xi^*_1)\cdot M_1(\xi^*_1)$ can be calculated by substituting them into each M_k.

Type-B period-2 orbits satisfy the condition

$$\begin{aligned}\tilde{\mathbf{v}}_0 &= \tilde{\mathbf{v}}_2 = (\tilde{v}^*_x, \tilde{v}^*_y, \tilde{v}^*_z), \\ \tilde{\mathbf{v}}_1 &= (\tilde{v}^*_x, -\tilde{v}^*_y, \tilde{v}^*_z).\end{aligned}$$

Similar to type-A orbits, we can obtain $\tilde{\mathbf{v}}_k$ and $\tilde{\mathbf{v}}''_k$ as a function of ξ^*_1. In addition, we can substitute

$$\xi^*_2 = \frac{1}{\alpha'}\ln\left[\frac{1 + (\tilde{v}_{z''})_1}{1 - (\tilde{v}_{z''})_1}\right] \tag{C26}$$

into the monodromy matrix to obtain $M(\xi^*_1)$.

Figure 11 shows the behavior of the trace of the monodromy matrix for the $(2)^{+(k)}$, where all the $(2)^{+(k)}$ orbits are

born stable and go through a period doubling bifurcation to $-\infty$. The degree of special relativity has a larger effect on orbits with a larger index k. We note that, for the type-B orbits $(2)^{-(k)}$ and $(2)^{*(k)}$, the behavior of the trace of their monodromy matrices is similar to Fig. 15 in Ref. [28]. All $(2)^{-(k)}$ orbits are still unstable for all dynamic parameters, as the periodic orbits associated with the superscript "–." All $(2)^{*(k)}$ orbits are born stable and can undergo a period-doubling and an inverse period-doubling bifurcation depending on the magnitude of the values of θ and $\theta^{\dagger}$, and eventually become unstable with a pitchfork bifurcation at $\mathrm{Tr}[M] = 2$.

APPENDIX D: PERIODIC ORBITS IN DOUBLE-BARRIER DYNAMICS

1. Period-1 orbits

a. Quantitative description

When the particle motion or trajectory involves elastic collisions with both the left and right barriers, periodic orbits can still be defined with respect to the left barrier in the Poincaré surface of section. In particular, a period-n orbit has n points in the Poincaré surface of section at $z = 0$. For $\theta \neq 0$, traversing motion is not sufficient for forming a period-1 orbit. Period-n orbits associated with helical motion can be denoted as $\{n, k\}$, which can be further refined based on the number of collisions with the right barrier within one period: $(m, n)^{\pm(k)}$ represents the periodic orbit $\{n, k\}$ colliding with the right barrier m times within one period for $0 \leqslant m \leqslant n$ ($m = 0$ or n for $\theta = 0$). The left barrier periodic orbits can then be denoted as $(0, n)^{\pm(k)}$ and all the others are the "right-barrier" periodic orbits. By this convention, period-1 orbits can be divided into two classes: $(0, 1)^{\pm(k)}$ and $(1, 1)^{\pm(k)}$ associated, respectively, with the left and right barriers.

As $1/\alpha$ changes through $1/\alpha^{\dagger}$, the left- and right-barrier periodic orbits simultaneously appear via a cusp bifurcation or mutually switch through a connectivity transition that is in fact not a bifurcation, as there is no new orbits emerge at the transition. The left-barrier period-1 orbits $(0, 1)^{\pm(k)}$ are the same as $(1)^{\pm(k)}$ from single-barrier dynamics with the same system parameters and the right-barrier period-1 orbits $(1, 1)^{\pm(k)}$ are quantitatively similar to the period-2 orbits in single-barrier dynamics. In particular, the first and the second segments of a $(1, 1)^{\pm(k)}$ orbit can be regarded as the first and second segments of a period-2 orbit from single-barrier dynamics: each containing motion in the space and a collision with the left barrier. For the $(1, 1)^{\pm(k)}$ orbits, the two segments without any collision with a barrier associated with ξ_r and ξ_l must have the same distance (not the displacement) along the z'' axis:

$$z'' = 0 \xrightarrow{\xi_r} z''(\xi_r) \xrightarrow{\xi_l} 0, \tag{D1}$$

which is an additional constraint for the period-2 orbits in the single-barrier dynamics. Only type-A period-2 orbits can meet this constraint, where zero mixing means that $(1, 1)^{\pm(k)}$ will have a point on the line $\widetilde{v}_y = 0$ - the same as $(0, 1)^{\pm(k)}$.

Qualitatively, a period-1 orbit in the single-barrier dynamics has two parts: one with $\widetilde{v}_{z''} \leqslant \widetilde{v}^{\dagger}_{z''}$ that becomes a $(0, 1)^{\pm(k)}$ orbit and the other with $\widetilde{v}^{\dagger}_{z''} < \widetilde{v}_{z''} < \widetilde{v}''_0$ that is cut off and then transforms into a $(1, 1)^{\pm(k)}$ orbit due to the right barrier.

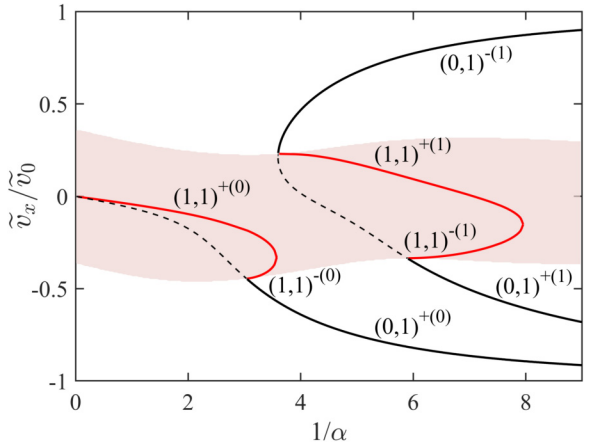

FIG. 12. Bifurcation behaviors of period-1 orbits from double-barrier dynamics in the coordinates $(1/\alpha, \widetilde{v}_x/\widetilde{v}_0)$. The parameters are $\widetilde{v}_0 = 0.8$ and $\theta = \pi/18$, and $\varrho = 1.2$. The black solid traces represent the orbits $(0, 1)^{+(0)}$ and $(0, 1)^{\pm(1)}$, the red solid traces represent the $(1, 1)^{\pm(k)}$ orbits with $k = 0, 1$, the black solid and dashed traces constitute the $(1)^{+(0)}$ and $(1)^{\pm(1)}$ orbits together, and the' pink region represents the intersecting area between the critical boundary and $\widetilde{v}_y = 0$.

Figure 12 shows the $(0, 1)^{\pm(k)}$ orbits as marked by black solid traces belonging to one part of the $(1)^{\pm(k)}$, and $(1, 1)^{\pm(k)}$ as marked by red solid traces coming from the transformation of the other part (marked by black dashed lines) of the $(1)^{\pm(k)}$. Overall, the requirement for the $(1, 1)^{\pm(k)}$ orbits is

$$\widetilde{v}_{y''} = -\tan\theta' \widetilde{v}_{z''}, \ \widetilde{v}_{y''}(\xi_r^-) = -\tan\theta' \widetilde{v}_{z''}(\xi_r^-). \tag{D2}$$

Similar to the solution procedure for type-A period-2 orbits in the single-barrier dynamics, $\mathcal{F}_{\pm}$ and $\mathcal{S}_{\pm}$ are functions of ξ and $\widetilde{v}_{z''}$. The following equations can be numerically solved

$$\begin{cases} \mathcal{F}_{\pm}(\xi, \widetilde{v}_{z''}) = (1 - 1/\gamma'_0)/\varrho' \cos\theta', \\ \mathcal{S}_{\pm}(\xi, \widetilde{v}_{z''}) = 0, \end{cases}, \tag{D3}$$

whose solution sets constitute the root set $\{(\xi_r^*, \widetilde{v}^*_{z''})\}$ together, where ξ_r^* is the first positive real root

$$\mathcal{F}_{\pm}(\xi, \widetilde{v}^*_{z''}) = (1 - 1/\gamma'_0)/\varrho' \cos\theta'.$$

As θ increases, the interval in q/α in which the $(1, 1)^{\pm(k)}$ orbits with $k > 0$ exist becomes narrower, which can be seen, as follows. The intersecting area (the pink region in Fig. 12) between the critical boundary and line $\widetilde{v}_y = 0$ is the region for $(1, 1)^{\pm(k)}$ orbits to exist, but the $(1)^{\pm(k)}$ orbits are cut off in this region. For a larger value of θ, this region shrinks and even disappear due to the movement of the critical boundary. Note that this analysis does not apply to the $(1, 1)^{+(0)}$ orbit, as the $(1, 1)^{+(0)}$ orbits exist even for small value of $1/\alpha$, analogous to the traversing motion for the untitled system, as the limit of $1/\alpha \to 0$ corresponds to the case of a vanishing magnetic field so that the value of θ has no effect on the orbits that can always reach the right barrier. In this sense, the $(0, 1)^{+(0)}$ orbit corresponds to deformed traversing motion for $\theta = 0$, denoted by the superscript "+," and it disappears with $(1, 1)^{-(0)}$ by a backward saddle-node bifurcation at a larger value of $1/\alpha$.

For $k > 0$, the $(0, 1)^{+(k)}$ orbits come form a saddle-node bifurcation along with the $(0, 1)^{-(k)}$ orbit, and the $(0, 1)^{+(k)}$

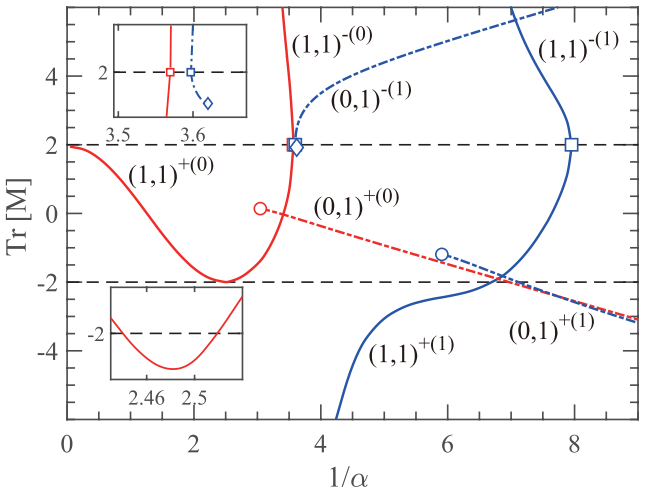

FIG. 13. Trace of the monodromy matrix for period-1 orbits in double-barrier dynamics. The parameter values are $\widetilde{v}_0 = 0.8$, $\theta = \pi/18$, and $\varrho = 1.2$. The red solid and dot-dashed curves represent the matrix trace for the $(1, 1)^{\pm(0)}$ and $(0, 1)^{+(0)}$ orbits and the blue solid and dot-dashed curves denote the trace of the matrix for the $(1, 1)^{\pm(1)}$ and $(0, 1)^{\pm(1)}$ orbits. The hollow rectangles, diamonds, and cycles represent the saddle-node bifurcation, connectivity transition, and cusp bifurcation, respectively. The subfigures are magnifications.

orbits cross the critical boundary at a larger value of $1/\alpha$ and become a $(1, 1)^{+(k)}$ orbit with a connectivity transition. As $1/\alpha$ increases further, the $(0, 1)^{+(k)}$ and $(1, 1)^{-(k)}$ orbits simultaneously appear at a cusp bifurcation, and a stable-unstable periodic orbit pair $(1, 1)^{\pm(k)}$ disappears through a backward saddle-node bifurcation, where the junctions between the $(1, 1)^{\pm(k)}$ and $(0, 1)^{+(k)}$ orbits represent the discontinuity when they cross the critical boundary. Hence, the right barrier orbits always emerge as the left barrier orbits cross the critical boundary, as shown in Fig. 12. Indeed, their evolutionary process is inherited from that for $\theta = 0$, as shown in Fig. 4): the left- and right-barrier orbits simultaneously appear at $\alpha = \alpha^{\dagger}$ and then the right-barrier orbits disappear at $\alpha = \alpha_{\rm TO}$. Intuitively, the bifurcation behaviors of the period-1 orbits from double-barrier dynamics are pieced together at the discontinuity by two behaviors in a pure single-barrier mapping $\boldsymbol{\mathcal{V}}''$ and a pure double-barrier mapping $\boldsymbol{\mathcal{V}}''_{\rm D}$ in the increasing and decreasing directions of $1/\alpha$, respectively.

b. Stability

The stability of period-1 orbits from double-barrier dynamics is determined by the $(0, 1)^{\pm(k)}$ orbit, which is the same as that of the $(1)^{\pm(k)}$ orbits with $\widetilde{v}_{z''} \leqslant \widetilde{v}^{\dagger}_{z''}$. The monodromy matrix for $(1, 1)^{\pm(k)}$ is $M = M_0 \cdot M_1$, where M_0 and M_1 are the monodromy matrices of the mappings $\boldsymbol{\mathcal{V}}''(\widetilde{\mathbf{v}}''; \xi_r)$ and $\boldsymbol{\mathcal{V}}''(\widetilde{\mathbf{v}}''_r; \xi_l)$ in the first and second segments, where $\widetilde{\mathbf{v}}''$ is the initial scaled velocity and $\widetilde{\mathbf{v}}''_r$ is the scaled velocity immediately after the collision with the right barrier. Note that Tr$[M]$ has singularities at the critical boundary and is not unique at those intersections (associated with the cusp bifurcation and the connectivity transition) of $(1, 1)^{\pm(k)}$ and $(0, 1)^{+(k)}$, as shown in Fig. 13. The behavior of Tr$[M]$ for period-1 orbits from double-barrier dynamics is similar to that of the corresponding orbits in the nonrelativistic regime.

2. Period-2 orbits

Similar to the origin of period-1 orbits, one part of the $(2)^{\pm(k)}$ and $(2)^{*(k)}$ orbits from single-barrier dynamics will become $(0, 2)^{\pm(k)}$ and $(0, 2)^{*(k)}$, leaving two points outside the critical boundary. The other part is cut off by the right barrier and deforms into $(1, 2)^{\pm(k)}$ or $(1, 2)^{\pm(k)}_{*}$ or $(2, 2)^{\pm(k)}$, depending on the number of collisions with the right barrier in one period, where the subscript "$*$" represents the orbits deformed from $(2)^{*(k)}$. As a result, all the right barrier period-2 orbits emerge through a cusp bifurcation or a connectivity transition. As Tr$[M]$ for the period-1 orbits crosses -2, the right-barrier period-2 orbits disappear as the $(1, 1)^{+(k)}$ goes through a backward period-doubling or inverse period-doubling bifurcation, which can be found by examining the corresponding deformed periodic orbits from the single-barrier dynamics.

To describe the deformation of the $(2)^{\pm(k)}$ and $(2)^{*(k)}$ orbits, we show a special property of the motion without collision in O'': if

$$\widetilde{\mathbf{v}}''_0 = \big(\widetilde{v}^0_{x''}, \widetilde{v}^0_{y''}, \widetilde{v}^0_{z''}\big) \xrightarrow{\xi_i} \widetilde{\mathbf{v}}''_1 = \big(\widetilde{v}^1_{x''}, \widetilde{v}^1_{y''}, \widetilde{v}^1_{z''}\big), \tag{D4}$$

then another such motion with the initial scaled velocity $(\widetilde{v}^1_{x''}, -\widetilde{v}^1_{y''}, -\widetilde{v}^1_{z''})$ and the motion parameter ξ_i will have the final scaled velocity (FSV) as

$$\big(\widetilde{v}^0_{x''}, -\widetilde{v}^0_{y''}, -\widetilde{v}^0_{z''}\big), \tag{D5}$$

or

$$\big(\widetilde{v}^1_{x''}, -\widetilde{v}^1_{y''}, -\widetilde{v}^1_{z''}\big) \xrightarrow{\xi_i} \big(\widetilde{v}^0_{x''}, -\widetilde{v}^0_{y''}, \widetilde{v}^0_{z''}\big). \tag{D6}$$

Proof: Eq. (D6) can be written as

$$\begin{aligned}
\widetilde{v}^1_{x''} &= \big(\widetilde{v}^0_{x''}\cos\xi_i - \widetilde{v}^0_{y''}\sin\xi_i\big)\gamma''_0/\gamma''_1,\\
\widetilde{v}^1_{y''} &= \big(\widetilde{v}^0_{y''}\cos\xi_i + \widetilde{v}^0_{x''}\sin\xi_i\big)\gamma''_0/\gamma''_1,\\
\widetilde{v}^1_{z''} &= \big[\cosh(\alpha'\xi_i)\widetilde{v}^0_{x''} - \sinh(\alpha'\xi_i)\big]\gamma''_0/\gamma''_1,
\end{aligned} \tag{D7}$$

leading to

$$\begin{aligned}
(\mathrm{FSV})_{\mathrm{x}} &= \big(\widetilde{v}^1_{x''}\cos\xi_i + \widetilde{v}^1_{y''}\sin\xi_i\big)\gamma''_1/\gamma''_0 = \widetilde{v}^0_{x''},\\
(\mathrm{FSV})_{\mathrm{y}} &= \big(-\widetilde{v}^1_{y''}\cos\xi_i + \widetilde{v}^1_{x''}\sin\xi_i\big)\gamma''_1/\gamma''_0 = -\widetilde{v}^0_{y''},\\
(\mathrm{FSV})_{\mathrm{z}} &= -\big[\cosh(\alpha'\xi_i)\widetilde{v}^1_{x''} + \sinh(\alpha'\xi_i)\big]\gamma''_1/\gamma''_0\\
&= -\widetilde{v}^0_{z''},
\end{aligned} \tag{D8}$$

which holds in the reference frame O' with $''$ replaced by $'$.

a. Deformed $(2)^{+(k)}$ orbits

The orbits $(2, 2)^{+(k)}$ deformed from the type-A period-2 orbits $(2)^{+(k)}$ are nonmixing for two collisions with the left barrier, i.e., the velocity is perpendicular to the left barrier immediately before such a collision. The scaled velocity in O' is

$$\begin{aligned}
&(\widetilde{v}_{x'}, 0, \widetilde{v}_{z'}) \xrightarrow{\xi_{1r}} \big(\widetilde{v}^r_{x'}, \widetilde{v}^r_{y'}, -\widetilde{v}^r_{z'}\big) \xrightarrow{1\mathrm{REC}} \big(\widetilde{v}^r_{x'}, \widetilde{v}^r_{y'}, \widetilde{v}^r_{z'}\big) \xrightarrow{\xi_{1l}}\\
&\big(\widetilde{v}^l_{x'}, 0, -\widetilde{v}^l_{z'}\big) \xrightarrow{1\mathrm{LEC}} \big(\widetilde{v}^l_{x'}, 0, \widetilde{v}^l_{z'}\big) \xrightarrow{\xi_{2r}=\xi_{1l}} \big(\widetilde{v}^r_{x'}, -\widetilde{v}^r_{y'}, -\widetilde{v}^r_{z'}\big)\\
&\xrightarrow{2\mathrm{REC}} \big(\widetilde{v}^r_{x'}, -\widetilde{v}^r_{y'}, \widetilde{v}^r_{z'}\big) \xrightarrow{\xi_{2l}=\xi_{1r}} (\widetilde{v}_{x'}, 0, -\widetilde{v}_{z'})\\
&\xrightarrow{2\mathrm{LEC}} (\widetilde{v}_{x'}, 0, \widetilde{v}_{z'}),
\end{aligned} \tag{D9}$$

where 1REC (2REC) denotes the first (second) elastic collision with the right barrier. The two points on the Poincaré surface of section in O' at $z' = 0$ are $(\widetilde{v}_{x'}, 0)$ and $(\widetilde{v}^{l}_{x'}, 0)$, and the corresponding points on the Poincaré section at $z' = d'$ are $(\widetilde{v}^{r}_{x'}, \widetilde{v}^{r}_{y'})$ and $(\widetilde{v}^{r}_{x'}, -\widetilde{v}^{r}_{y'})$. After a Lorentz transformation, in the frame O there are two points on the line $\widetilde{v}_y = 0$ at the left barrier and two points that are symmetrical about this line at the right barrier, which are characteristic of type-A orbits.

There are four motion segments without a collision. Applying Eq. (D8) twice to ensure the same velocity immediately after the second collision with the left barrier as the initial velocity leads to the period-2 orbits. A requirement is that the orbits be nonmixing for the two collisions with the left barrier. In particular, for the $(2, 2)^{+(k)}$ orbits, we have

$$\begin{aligned} \widetilde{v}_{y''} &= -\tan\theta' \widetilde{v}_{z''}, \\ \widetilde{v}_{y''}(\xi_{1r} + \xi^{-}_{1l}) &= -\tan\theta' \widetilde{v}_{z''}(\xi_{1r} + \xi^{-}_{1l}). \end{aligned} \tag{D10}$$

The quantities $\mathcal{F}_{\pm}$ and $\mathcal{S}_{\pm}$ as a function of ξ_{1r} and $\widetilde{v}_{z''}$. The following equations can be numerically solved:

$$\begin{cases} \mathcal{F}_{\pm}(\xi_{1r}, \widetilde{v}_{z''}) = (1 - 1/\gamma'_0)/\varrho' \cos\theta' \\ \mathcal{S}_{\pm}(\xi_{1l}, \widetilde{\mathbf{v}}''_r) = 0 \end{cases} \tag{D11}$$

with ξ_{1r} and ξ_{1l} from Eqs. (27) and (30), respectively, $\widetilde{\mathbf{v}}''_r$ is the scaled velocity immediately after the first collision with the right barrier, and ξ_{1l} is also a function of ξ_{1r} and $\widetilde{v}_{z''}$ according to Eq. (30). The root set $\{(\xi^{*}_{1r}, \widetilde{v}^{*}_{z''})\}$ is the union of the solution sets.

The $(2, 2)^{+(0)}$ and $(0, 2)^{+(0)}$ orbits simultaneously emerge through a cusp bifurcation. As $1/\alpha$ increases, the orbit $(2, 2)^{+(0)}$ disappears via a backward period-doubling bifurcation when $\mathrm{Tr}[M]$ of $(1, 1)^{+(0)}$ crosses -2 (left-bottom corner in Fig. 13), as shown in Fig. 14.

b. Deformed $(2)^{-(k)}$ and $(2)^{*(k)}$ orbits

The type-B period-2 orbits $(2)^{-(k)}$ and $(2)^{*(k)}$ from single-barrier dynamics are deformed into the $(2, 2)^{-(k)}$, $(1, 2)^{\pm(k)}$, and $(1, 2)^{\pm(k)}_{*}$ orbits in double-barrier dynamics. All these orbits are nonmixing for the right barrier and self-retracing for the left barrier. We first consider the $(2, 2)^{-(k)}$ orbits in O':

$$\begin{aligned} (\widetilde{v}_{x'}, \widetilde{v}_{y'}, \widetilde{v}_{z'}) &\xrightarrow{\xi_{1r}} (\widetilde{v}^{r}_{x'}, 0, -\widetilde{v}^{r}_{z'}) \xrightarrow{\text{1REC}} (\widetilde{v}^{r}_{x'}, 0, \widetilde{v}^{r}_{z'}) \xrightarrow{\xi_{1l}=\xi_{1r}} \\ (\widetilde{v}_{x'}, -\widetilde{v}_{y'}, -\widetilde{v}_{z'}) &\xrightarrow{\text{1LEC}} (\widetilde{v}_{x'}, -\widetilde{v}_{y'}, \widetilde{v}_{z'}) \xrightarrow{\xi_{2r}} (\widetilde{v}^{r_2}_{x'}, 0, -\widetilde{v}^{r_2}_{z'}) \\ &\xrightarrow{\text{2REC}} (\widetilde{v}^{r_2}_{x'}, 0, \widetilde{v}^{r_2}_{z'}) \xrightarrow{\xi_{2l}=\xi_{2r}} (\widetilde{v}_{x'}, \widetilde{v}_{y'}, -\widetilde{v}_{z'}) \\ &\xrightarrow{\text{2LEC}} (\widetilde{v}_{x'}, \widetilde{v}_{y'}, \widetilde{v}_{z'}), \end{aligned} \tag{D12}$$

The two points at the left barrier are $(\widetilde{v}_{x'}, \widetilde{v}_{y'})$ and $(\widetilde{v}_{x'}, -\widetilde{v}_{y'})$, and the corresponding points at the right barrier are $(\widetilde{v}^{r}_{x'}, 0)$ and $(\widetilde{v}^{r_2}_{x'}, 0)$. These points are different from those from the $(2, 2)^{+(k)}$ orbits: at the left barrier the two points are symmetrical about the line $\widetilde{v}_y = 0$r and, at the right barrier, the two points are on the line $\widetilde{v}_y = 0$. They constitute type-B orbits on the Poincaré surface of section at $z = 0$.

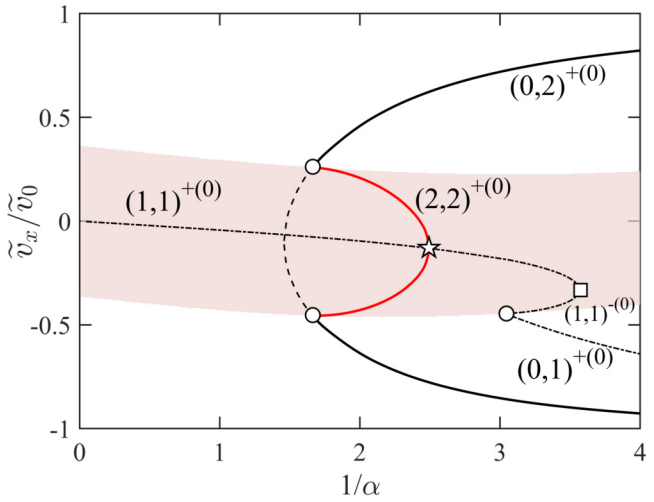

FIG. 14. Bifurcation behavior for the period-2 orbits from double-barrier dynamics. The orbits are $(2, 2)^{+(0)}$ and $(0, 2)^{+(0)}$. The parameter values are $\widetilde{v}_0 = 0.8$, $\theta = \pi/18$, and $\varrho = 1.2$. The black dash-dotted, black solid, and red curves represent the period-1 orbits $\{1, 0\}$, $(0, 2)^{+(0)}$, and $(2, 2)^{+(0)}$, respectively. The black solid and dashed curves constitute the $(2)^{+(0)}$ orbit from single-barrier dynamics. The hollow rectangles, pentagrams and cycles represent the saddle-node, backward period-doubling and cusp bifurcations, respectively.

For the $(2, 2)^{-(k)}$ orbits, the velocity is perpendicular to the right barrier immediately before each collision with the right barrier:

$$\begin{aligned} \widetilde{v}_{y''}(\xi^{-}_{1r}) &= -\tan\theta' \widetilde{v}_{z''}(\xi^{-}_{1r}), \\ \widetilde{v}_{y''}(2\xi_{1r} + \xi^{-}_{2r}) &= -\tan\theta' \widetilde{v}_{z''}(2\xi_{1r} + \xi^{-}_{2r}), \end{aligned} \tag{D13}$$

where ξ_{1r} is obtained by Eq. (27), and ξ_{2r} is the first positive real root of the equation

$$\mathcal{F}(\xi, \widetilde{\mathbf{v}}''_l) = (1 - 1/\gamma'_0)/\varrho' \cos\theta'.$$

Immediately after the second collision with the left barrier in O', the scaled velocity $\widetilde{\mathbf{v}}'_l = (\widetilde{v}_{x'}, -\widetilde{v}_{y'}, \widetilde{v}_{z'})$ in O'' is

$$\begin{aligned} \widetilde{\mathbf{v}}''_l = (&\widetilde{v}_{x''}, -\widetilde{v}_{y''} \cos 2\theta' - \widetilde{v}_{z''} \sin 2\theta', \\ &- \widetilde{v}_{y''} \sin 2\theta' + \widetilde{v}_{z''} \cos 2\theta'). \end{aligned} \tag{D14}$$

For simplicity, we choose $\widetilde{v}^{r}_{z''}$ as one of the independent variables, and equivalently replace the process

$$(\widetilde{v}_{x'}, \widetilde{v}_{y'}, \widetilde{v}_{z'}) \xrightarrow{\xi_{1r}} (\widetilde{v}^{r}_{x'}, 0, -\widetilde{v}^{r}_{z'})$$

by

$$(\widetilde{v}^{r}_{x'}, 0, \widetilde{v}^{r}_{z'}) \xrightarrow{\xi_{1l}=\xi_{1r}} (\widetilde{v}_{x'}, -\widetilde{v}_{y'}, -\widetilde{v}_{z'}).$$

Similar to the $(2, 2)^{+(k)}$ orbits, $\widetilde{v}^{r}_{z''}$ and ξ_{1l} are independent variables. We can solve

$$\begin{cases} \mathcal{F}_{\pm}(\xi_{1l}, \widetilde{v}^{r}_{z''}) = (1 - \gamma'_0)/\varrho' \cos\theta' \gamma'(\xi_{1r}), \\ \mathcal{S}_{\pm}(\xi_{2r}, \widetilde{\mathbf{v}}''_l) = 0, \end{cases} \tag{D15}$$

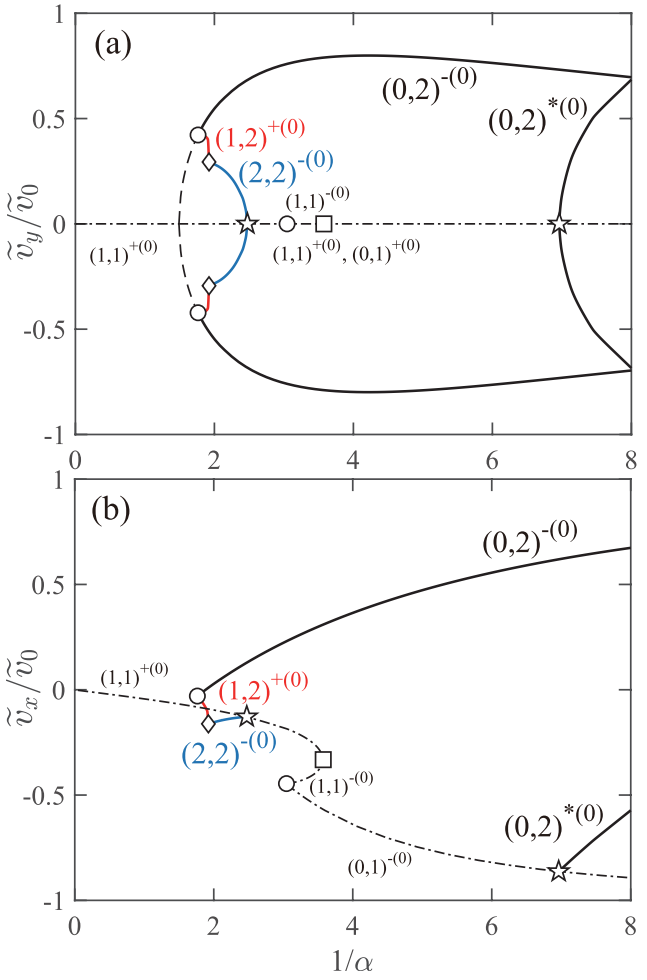

FIG. 15. Bifurcation behavior of the $(2,2)^{-(0)}$, $(1,2)^{+(0)}$, $(0,2)^{-(0)}$, and $(0,2)^{*(0)}$ orbits from double-barrier dynamics. (a) $\widetilde{v}_y/\widetilde{v}_0$ and (b) $\widetilde{v}_x/\widetilde{v}_0$ vs $1/\alpha$. The parameters are $\widetilde{v}_0 = 0.8$, $\theta = \pi/18$, and $\varrho = 1.2$. The rectangles, pentagrams, cycles, and diamonds represent the saddle-node, period-doubling (or backward inverse period-doubling), cusp bifurcations, and connectivity transition, respectively.

where

$$1/\gamma'(\xi_{1r}) = [\cosh(\alpha'\xi_{1l}) - \sinh(\alpha'\xi_{1l})\widetilde{v}^r_{z''}]/\gamma'_0.$$

Moreover, $\widetilde{v}^r_{x''}(\widetilde{v}^r_{z''})$ can be obtained by replacing γ_0 and $\widetilde{v}_{z''}$ with γ_r and $\widetilde{v}^r_{z''}$ into $\widetilde{v}_{x''}(\widetilde{v}_{z''})$, respectively.

In the frame O', the changes in the scaled velocity for the $(1,2)^{\pm(k)}$ and $(1,2)^{\pm(k)}_*$ are

$$\begin{aligned}(\widetilde{v}_{x'}, \widetilde{v}_{y'}, \widetilde{v}_{z'}) &\xrightarrow{\xi_1} (\widetilde{v}_{x'}, -\widetilde{v}_{y'}, -\widetilde{v}_{z'}) \xrightarrow{\text{1LEC}} (\widetilde{v}_{x'}, -\widetilde{v}_{y'}, \widetilde{v}_{z'}) \\ &\xrightarrow{\xi_{2r}} (\widetilde{v}^r_{x'}, 0, -\widetilde{v}^r_{z'}) \xrightarrow{\text{1REC}} (\widetilde{v}^r_{x'}, 0, \widetilde{v}^r_{z'}) \xrightarrow{\xi_{2l}=\xi_{2r}} \\ (\widetilde{v}_{x'}, \widetilde{v}_{y'}, -\widetilde{v}_{z'}) &\xrightarrow{\text{2LEC}} (\widetilde{v}_{x'}, \widetilde{v}_{y'}, \widetilde{v}_{z'}). \end{aligned} \tag{D16}$$

In particular, ξ_{2r} does not exist, ξ_{2l} degenerates into ξ_2, and ξ_1 splits into ξ_{1r} and ξ_{1l} owing to the collision with the right barrier. This process includes three motion segments without any collision. There is only one point on the Poincaré section at the right barrier.

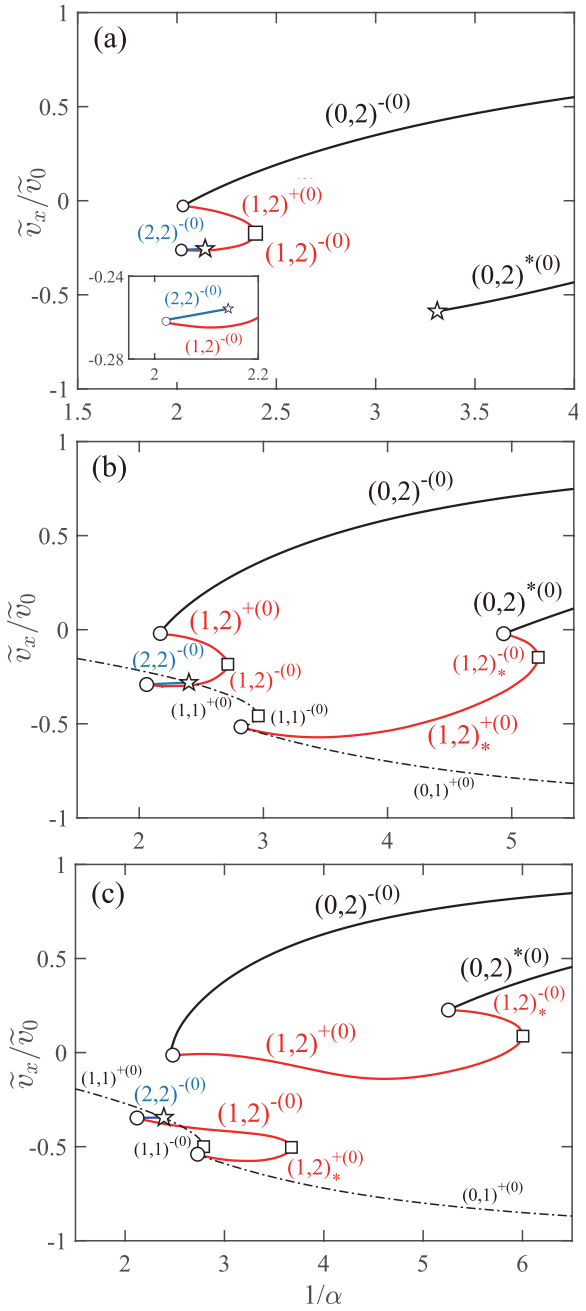

FIG. 16. Bifurcations from the $(2)^{-(k)}$ and $(2)^{*(k)}$ orbits with the tilted angle increases in double-barrier dynamics. [(a)–(c)] bifurcation of the $(2,2)^{-(0)}$, (1,2), $(0,2)^{-(0)}$, and $(0,2)^{*(0)}$ orbits in regimes 2-4, respectively. The parameters are $\widetilde{v}_0 = 0.8$ and $\varrho = 1.2$ for (a) $\theta = \pi/9$, (b) $\theta = \pi/7.7$, and (c) $\theta = \pi/6$. The rectangles, pentagrams and cycles represent the saddle-node, period-doubling (or backward inverse period-doubling), and cusp bifurcations, respectively.

The motion segment without any collision with the parameter ξ_1 is self-retracing, implying

$$\begin{aligned}\widetilde{v}_{z''} &= \frac{\exp(\alpha'\xi_1) - 1}{\exp(\alpha'\xi_1) + 1}, \\ \widetilde{v}_{y''} &= -\widetilde{v}_{x''}\tan(\xi_1/2), \end{aligned} \tag{D17}$$

without involving ξ_{1r}. For type-B orbits, $\tilde{v}_{x''}$ is a function of ξ_1, and we have $\tilde{\mathbf{v}}''(\xi_1)$ and $\tilde{\mathbf{v}}_l''(\xi_1)$. In addition to requiring that the velocity be perpendicular to the right barrier immediately before the first collision, we further solve

$$\begin{cases} \mathcal{F}_{\pm}(\xi_{2r}, \tilde{\mathbf{v}}_l'') = (1 - 1/\gamma_0')/\varrho' \cos\theta' \\ \mathcal{S}_{\pm}(\xi_{2r}, \tilde{\mathbf{v}}_l'') = 0 \end{cases}, \tag{D18}$$

where ξ_{2r} is the first positive real root of

$$\mathcal{F}_{\pm}(\xi, \tilde{\mathbf{v}}_l'') = (1 - 1/\gamma_0')/\varrho' \cos\theta'.$$

The bifurcations from the $(2)^{-(k)}$ and $(2)^{*(k)}$ orbits as the tilted angle increases have four distinct behaviors: *regime one* ($\theta < \hat{\theta}_1$), *regime two* ($\hat{\theta}_1 < \theta < \hat{\theta}_2$), *regime three* ($\hat{\theta}_2 < \theta < \hat{\theta}^{\dagger}$), and *regime four* ($\hat{\theta}^{\dagger} < \theta$), which are described, as follows.

Regime one. As shown in Fig. 15, as $1/\alpha$ increases, the $(1,2)^{+(0)}$ and $(0,2)^{-(0)}$ orbits emerge through a cusp bifurcation, and $(1,2)^{+(0)}$ then becomes $(2,2)^{-(0)}$ through a connectivity transition. As $1/\alpha$ reaches the value corresponding to the first intersection of Tr[M] for $(1,1)^{+(0)}$ and -2, the $(2,2)^{-(0)}$ orbit disappears through a backward inverse period-doubling bifurcation. However, there is no deformation of $(2)^{*(0)}$, because it cannot reach the right barrier even for sufficiently large values of $1/\alpha$. The $(2)^{-(k)}$ and $(2)^{*(k)}$ orbits can deform into the orbits in the form (1,2), different from $(2)^{+(k)}$. What happens instead is that the $(0,2)^{-(k)}$ orbit is born in a cusp bifurcation with $(1,2)^{+(k)}$ instead of the type of (2,2), because $\xi_1 \neq \xi_2$ for type-B period-2 orbits and one of ξ_1 and ξ_2 is always destroyed by the right barrier by breaking into two motion segments without a collision: denoted as ξ_{ir} and ξ_{il} with $i = 1$ or 2 near the critical boundary. Note that, for the type-A orbits $(2)^{+(k)}$, ξ_1 and ξ_2 are equal so they are destroyed at the same $1/\alpha$ value.

Regime two. As shown in Fig. 16(a), the $(2)^{*(0)}$ orbit has still not been deformed but a new orbit has emerged: $(1,2)^{-(0)}$. In fact, the $(1,2)^{+(0)}$ and $(0,2)^{-(0)}$ orbits are created through a cusp bifurcation, so are the $(1,2)^{-(0)}$ and $(2,2)^{-(0)}$ orbits. As $1/\alpha$ increases further, a stable-unstable periodic orbit pair $(1,2)^{\pm(0)}$ is destroyed through a backward saddle-node bifurcation, similar to the disappearance of the $(1,1)^{\pm(k)}$ orbits. The $(2,2)^{-(0)}$ orbit goes through the same process as in regime one until it disappears.

Regime three. The deformation of the $(2)^{-(0)}$ orbit is the same as in regime two. As the tilted angle increases, the $(2)^{*(0)}$ orbit begins to deform and new orbits $(1,2)_*^{\pm(0)}$ are born, as shown in Fig. 16(b). The $(1,2)_*^{+(0)}$ orbit is created through a cusp bifurcation, where $(0,1)^{+(0)}$ and $(1,1)^{-(0)}$ emerge through the same cusp bifurcation, indicating that the new periodic orbits are always born at the critical boundary. In addition, the $(1,2)_*^{-(0)}$ and $(0,2)^{*(0)}$ orbits appear through a cusp bifurcation and then an orbit pair $(1,2)_*^{\pm(0)}$ is destroyed through a backward saddle-node bifurcation. The bifurcation behaviors in regime three bear certain similarities to those of type-B period-2 orbits in single-barrier dynamics [Fig. 9(b)], where the third intersection of Tr[M] for $(1)^{+(0)}$ with -2 is close to the second one.

Regime four. This regime corresponds to the case of $\theta > \theta^{\dagger}$ in single-barrier dynamics [Fig. 9(c)], where the $(2)^{-(k)}$ orbit is connected to $(2)^{*(k)}$ by a saddle-node bifurcation from an inverse period-doubling bifurcation and the second period-doubling bifurcation for $(1)^{+(k)}$. In double-barrier dynamics, a similar connection occurs for $(1,2)^{\pm(k)}$ and $(1,2)_*^{\pm(k)}$ via an "exchange of partners" bifurcation, where two backward saddle-node bifurcations in regime three are exchanged. In the corresponding nonrelativistic dynamics, this exchange phenomenon plays a dominant role in the tunneling spectrum [31–33]. Figure 16(c) shows that $(1,2)^{+(0)}$ and $(0,2)^{-(0)}$ emerge through a cusp bifurcation, so do $(1,2)_*^{-(0)}$ and $(0,2)^{*(0)}$. As $1/\alpha$ increases further, the $(1,2)^{+(0)}$ and $(1,2)_*^{-(0)}$ orbits are destroyed through a backward saddle-node bifurcation, and the same behavior occurs for the $(1,2)^{-(0)}$ and $(1,2)_*^{+(0)}$ orbits.

For a small tilted angle, the $(2,2)^{\pm(k)}$ orbits are dominant. As the angle increases, more (1,2) orbits emerge. A general observation is that the right-barrier period-n orbits always appear through a cusp bifurcation as the relevant left-barrier orbits cross the critical boundary.

[1] S. Katsura and W. Fukuda, Exactly solvable models showing chaotic behavior, Physica A **130**, 597 (1985).

[2] E. Ott, *Chaos in Dynamical Systems* (Cambridge University Press, Cambridge, UK, 1993).

[3] R. W. Rollins and E. R. Hunt, Exactly solvable model of a physical system exhibiting universal chaotic behavior, Phys. Rev. Lett. **49**, 1295 (1982).

[4] M. Olshanii, K. Jacobs, M. Rigol, V. Dunjko, H. Kennard, and V. A. Yurovsky, An exactly solvable model for the integrability–chaos transition in rough quantum billiards, Nat. Commun. **3**, 641 (2012).

[5] N. J. Corron, J. N. Blakely, and M. T. Stahl, A matched filter for chaos, Chaos **20**, 023123 (2010).

[6] N. J. Corron and J. N. Blakely, Exact folded-band chaotic oscillator, Chaos **22**, 023113 (2012).

[7] B. A. M. Owens, M. T. Stahl, N. J. Corron, J. N. Blakely, and L. Illing, Exactly solvable chaos in an electromechanical oscillator, Chaos **23**, 033109 (2013).

[8] J. N. Blakely and N. J. Corron, Correlation properties of exactly solvable chaotic oscillators, Phys. Rev. E **88**, 022909 (2013).

[9] N. J. Corron, R. M. Cooper, and J. N. Blakely, Analytically solvable chaotic oscillator based on a first-order filter, Chaos **26**, 023104 (2016).

[10] M. S. Milosavljevic, J. N. Blakely, A. N. Beal, and N. J. Corron, Analytic solutions throughout a period doubling route to chaos, Phys. Rev. E **95**, 062223 (2017).

[11] J. Blakely, M. Milosavljevic, and N. Corron, Timing variation in an analytically solvable chaotic system, Physica D **340**, 40 (2017).

[12] A. E. Kaplan, Hysteresis in cyclotron resonance based on weak relativistic-mass effects of the electron, Phys. Rev. Lett. **48**, 138 (1982).

[13] G. Gabrielse, H. Dehmelt, and W. Kells, Observation of a relativistic, bistable hysteresis in the cyclotron motion of a single electron, Phys. Rev. Lett. **54**, 537 (1985).

[14] A. A. Chernikov, T. Tél, G. Vattay, and G. M. Zaslavsky, Chaos in the relativistic generalization of the standard map, Phys. Rev. A **40**, 4072 (1989).

[15] J.-H. Kim and H.-W. Lee, Relativistic chaos in the driven harmonic oscillator, Phys. Rev. E **51**, 1579 (1995).

[16] H.-W. Lee, Relativistic chaos in time-driven linear and nonlinear oscillators, in *Chaos — The Interplay Between Stochastic and Deterministic Behaviour*, edited by P. Garbaczewski, M. Wolf, and A. Weron (Springer, Berlin, Heidelberg, 1995), pp. 503–506.

[17] J.-H. Kim and H.-W. Lee, Chaos in the relativistic cyclotron motion of a charged particle, Phys. Rev. E **54**, 3461 (1996).

[18] S. P. Drake, C. P. Dettmann, N. E. Frankel, and N. J. Cornish, Chaos in special relativistic dynamics, Phys. Rev. E **53**, 1351 (1996).

[19] F. Burnell, R. B. Mann, and T. Ohta, Chaos in a relativistic 3-body self-gravitating system, Phys. Rev. Lett. **90**, 134101 (2003).

[20] F. Burnell, J. J. Malecki, R. B. Mann, and T. Ohta, Chaos in an exact relativistic three-body self-gravitating system, Phys. Rev. E **69**, 016214 (2004).

[21] T. Kovács, G. Bene, and T. Tél, Relativistic effects in the chaotic Sitnikov problem, Month. Noti. Roy. Astrono. Soc. **414**, 2275 (2011).

[22] J. D. Bernal, J. M. Seoane, and M. A. F. Sanjuán, Global relativistic effects in chaotic scattering, Phys. Rev. E **95**, 032205 (2017).

[23] R. S. Vieira and T. A. Michtchenko, Relativistic chaos in the anisotropic harmonic oscillator, Chaos Solit. Fract. **117**, 276 (2018).

[24] H. Takabe, Chaos due to relativistic effect, in *The Physics of Laser Plasmas and Applications - Volume 1: Physics of Laser Matter Interaction* (Springer International Publishing, Cham, 2020), pp. 287–330.

[25] M. Przybylska, W. Szumiński, and A. J. Maciejewski, Destructive relativity, Chaos **33**, 063156 (2023).

[26] A. J. Lichtenberg and M. A. Lieberman, *Regular and Chaotic Dynamics* (Springer-Verlag, New York, 1994).

[27] Y.-C. Lai and T. Tél, *Transient Chaos - Complex Dynamics on Finite Time Scales* (Springer, New York, 2011).

[28] E. E. Narimanov and A. D. Stone, Theory of the periodic orbits of a chaotic quantum well, Phys. Rev. B **57**, 9807 (1998).

[29] D. L. Shepelyansky and A. D. Stone, Chaotic Landau level mixing in classical and quantum wells, Phys. Rev. Lett. **74**, 2098 (1995).

[30] E. E. Narimanov, A. D. Stone, and G. S. Boebinger, Semiclassical theory of magnetotransport through a chaotic quantum well, Phys. Rev. Lett. **80**, 4024 (1998).

[31] T. M. Fromhold, L. Eaves, F. W. Sheard, M. L. Leadbeater, T. J. Foster, and P. C. Main, Magnetotunneling spectroscopy of a quantum well in the regime of classical chaos, Phys. Rev. Lett. **72**, 2608 (1994).

[32] T. Fromhold, L. Eaves, F. Sheard, T. Foster, M. Leadbeater, and P. Main, Quantum chaos in resonant tunneling diodes, Phys. B: Condens. Matter **201**, 367 (1994).

[33] T. Fromhold, M. Leadbeater, L. Eaves, T. Foster, P. Main, and F. Sheard, Tunneling into classically chaotic orbits in quantum wells, Surf. Sci. **305**, 511 (1994).

[34] E. E. Narimanov and A. D. Stone, Origin of strong scarring of wave functions in quantum wells in a tilted magnetic field, Phys. Rev. Lett. **80**, 49 (1998).

[35] T. M. Fromhold, P. B. Wilkinson, F. W. Sheard, L. Eaves, J. Miao, and G. Edwards, Manifestations of classical chaos in the energy level spectrum of a quantum well, Phys. Rev. Lett. **75**, 1142 (1995).

[36] G. Müller, G. S. Boebinger, H. Mathur, L. N. Pfeiffer, and K. W. West, Precursors and transition to chaos in a quantum well in a tilted magnetic field, Phys. Rev. Lett. **75**, 2875 (1995).

[37] P. B. Wilkinson, T. M. Fromhold, L. Eaves, F. W. Sheard, N. Miura, and T. Takamasu, Evidence for periodic "scar" patterns in the wavefunctions of a chaotic quantum well, Surf. Sci. **361-362**, 696 (1996).

[38] P. B. Wilkinson, T. M. Fromhold, L. Eaves, F. W. Sheard, N. Miura, and T. Takamasu, Observation of 'scarred' wavefunctions in a quantum well with chaotic electron dynamics, Nature (London) **380**, 608 (1996).

[39] T. S. Monteiro and P. A. Dando, Chaos in a quantum well in tilted fields: a scaling system, Phys. Rev. E **53**, 3369 (1996).

[40] T. S. Monteiro, D. Delande, A. J. Fisher, and G. S. Boebinger, Bifurcations and the transition to chaos in the resonant-tunneling diode, Phys. Rev. B **56**, 3913 (1997).

[41] T. M. Fromhold, P. B. Wilkinson, F. W. Sheard, and L. Eaves, Comment on "Precursors and transition to chaos in a quantum well in a tilted magnetic field", Phys. Rev. Lett. **78**, 2865 (1997).

[42] D. Keefe, Collective-effect accelerators, Sci. Am. **226**, 22 (1972).

[43] D. Cesar, J. Maxson, X. Shen, K. Wootton, S. Tan, R. England, and P. Musumeci, Enhanced energy gain in a dielectric laser accelerator using a tilted pulse front laser, Opt. Express **26**, 29216 (2018).

[44] V. A. Froltsov, R. Blaak, C. N. Likos, and H. Löwen, Crystal structures of two-dimensional magnetic colloids in tilted external magnetic fields, Phys. Rev. E **68**, 061406 (2003).

[45] M. Reiser, *Theory and Design of Charged Particle Beams* (John Wiley & Sons, 2008).

[46] B. Büttner, C. Liu, G. Tkachov, E. Novik, C. Brüne, H. Buhmann, E. Hankiewicz, P. Recher, B. Trauzettel, S. Zhang *et al.*, Single valley Dirac fermions in zero-gap HgTe quantum wells, Nat. Phys. **7**, 418 (2011).

[47] J. D. Jackson, *Classical Electrodynamics* (John Wiley & Sons, New York, 1962).

[48] A. Taub, Orbits of charged particles in constant fields, Phys. Rev. **73**, 786 (1948).

[49] D. Hestenes, Proper particle mechanics, J. Math. Phys. **15**, 1778 (1974).

[50] N. Salingaros, Particle in an external electromagnetic field. II. The exact velocity in a constant and uniform field, Phys. Rev. D **31**, 3150 (1985).

[51] J. R. Zeni and W. A. Rodrigues, Jr., A thoughtful study of Lorentz transformations by Clifford algebras, Int. J. Mod. Phys. A **07**, 1793 (1992).

[52] A. T. Hyman, Relativistic charged-particle motion in a constant field according to the Lorentz force law, Am. J. Phys. **65**, 195 (1997).

[53] S. A. Chin, Relativistic motion in a constant electromagnetic field, J. Math. Phys. **50**, 012904 (2009).

[54] L. E. Reichl, *The Transition to Chaos in Conservative Classical Systems: Quantum Manifestations* (Springer-Verlag, New York, 1992).

[55] C. Grebogi, E. Ott, and J. A. Yorke, Unstable periodic orbits and the dimensions of multifractal chaotic attractors, Phys. Rev. A **37**, 1711 (1988).

[56] Y.-C. Lai, Y. Nagai, and C. Grebogi, Characterization of the natural measure by unstable periodic orbits in chaotic attractors, Phys. Rev. Lett. **79**, 649 (1997).

[57] Y.-C. Lai, Characterization of the natural measure by unstable periodic orbits in nonhyperbolic chaotic systems, Phys. Rev. E **56**, 6531 (1997).

[58] M. Dhamala and Y.-C. Lai, Unstable periodic orbits and the natural measure of nonhyperbolic chaotic saddles, Phys. Rev. E **60**, 6176 (1999).

[59] R. L. Davidchack and Y.-C. Lai, Efficient algorithm for detecting unstable periodic orbits in chaotic systems, Phys. Rev. E **60**, 6172 (1999).

[60] R. L. Davidchack, Y.-C. Lai, E. M. Bollt, and M. Dhamala, Estimating generating partitions of chaotic systems by unstable periodic orbits, Phys. Rev. E **61**, 1353 (2000).

[61] M. C. Gutzwiller, *Chaos in Classical and Quantum Mechanics* (Springer-Verlag, New York, 2013).

[62] S. Bleher, E. Ott, and C. Grebogi, Routes to chaotic scattering, Phys. Rev. Lett. **63**, 919 (1989).

[63] M. Ding, C. Grebogi, E. Ott, and J. A. Yorke, Transition to chaotic scattering, Phys. Rev. A **42**, 7025 (1990).

[64] Y.-C. Lai, C. Grebogi, R. Blümel, and M. Ding, Algebraic decay and phase-space metamorphoses in microwave ionization of hydrogen rydberg atoms, Phys. Rev. A **45**, 8284 (1992).

[65] Y.-C. Lai, C. Grebogi, R. Blümel, and I. Kan, Crisis in chaotic scattering, Phys. Rev. Lett. **71**, 2212 (1993).

[66] Y.-C. Lai, Abrupt bifurcation to chaotic scattering with discontinuous change in fractal dimension, Phys. Rev. E **60**, R6283 (1999).

[67] Y.-C. Lai, A. P. S. de Moura, and C. Grebogi, Topology of high-dimensional chaotic scattering, Phys. Rev. E **62**, 6421 (2000).